

1 Revision 1 - Word count: 9,889 (text)

2

3 **X-ray absorption spectroscopy study of Mn reference compounds**  
4 **for Mn speciation in terrestrial surface environments**

5 TERESA ZAHORANSKY<sup>a</sup>, ANNA V. WEGORZEWSKI<sup>b</sup>, WINNIE HUONG<sup>a</sup>, CHRISTIAN  
6 MIKUTTA<sup>a,\*</sup>

7 <sup>a</sup>Soil Mineralogy, Institute of Mineralogy, Gottfried Wilhelm Leibniz University Hannover,  
8 Callinstr. 3, D-30167 Hannover, Germany

9 <sup>b</sup>Federal Institute for Geosciences and Natural Resources (BGR), Stilleweg 2, D-30655 Han-  
10 nover, Germany

11

12

13

14

15

16

17 **\*Correspondence**

18 [c.mikutta@mineralogie.uni-hannover.de](mailto:c.mikutta@mineralogie.uni-hannover.de)

19

20

21 **Keywords**

22 Manganese, average oxidation state, speciation, X-ray absorption near edge structure  
23 (XANES) spectroscopy, extended X-ray absorption fine structure (EXAFS) spectroscopy,  
24 linear combination fitting, spectral fingerprinting, soils and sediments

25

26

## ABSTRACT

27 X-ray absorption spectroscopy (XAS) offers great potential to identify and quantify Mn spe-  
28 cies in surface environments by means of linear combination fit (LCF), fingerprint, and shell-  
29 fit analyses of bulk Mn XAS spectra. However, these approaches are complicated by the lack  
30 of a comprehensive and accessible spectrum library. Additionally, molecular-level infor-  
31 mation on Mn coordination in some potentially important Mn species occurring in soils and  
32 sediments is missing. Therefore, we investigated a suite of 32 natural and synthetic Mn refer-  
33 ence compounds, including Mn oxide, oxyhydroxide, carbonate, phosphate, and silicate min-  
34 erals, as well as organic and adsorbed Mn species, by Mn K-edge X-ray absorption near edge  
35 structure (XANES) and extended X-ray absorption fine structure (EXAFS) spectroscopy. The  
36 ability of XAS to infer the average oxidation state (AOS) of Mn was assessed by comparing  
37 XANES-derived AOS with the AOS obtained from redox titrations. All reference compounds  
38 were studied for their local ( $<5 \text{ \AA}$ ) Mn coordination environment using EXAFS shell-fit anal-  
39 ysis. Statistical analyses were employed to clarify how well and to what extent individual Mn  
40 species (groups) can be distinguished by XAS based on spectral uniqueness. Our results show  
41 that LCF analysis of normalized XANES spectra can reliably quantify the Mn AOS within  
42  $\sim 0.1$  v.u. in the range +2 to +4. These spectra are diagnostic for most Mn species investigated,  
43 but unsuitable to identify and quantify members of the manganate and Mn(III)-oxyhydroxide  
44 groups. First-derivative XANES fingerprinting allows the unique identification of pyrolusite,  
45 ramsdellite, and potentially lithiophorite within the manganate group. However, XANES  
46 spectra of individual Mn compounds can vary significantly depending on chemical composi-  
47 tion and/or crystallinity, which limits the accuracy of XANES-based speciation analyses. In  
48 contrast, EXAFS spectra provide a much better discriminatory power to identify and quantify  
49 Mn species. Principal component and cluster analyses of  $k^2$ -weighted EXAFS spectra of Mn  
50 reference compounds implied that EXAFS LCF analysis of environmental samples can identi-

51 fy and quantify at least the following primary Mn species groups: (1) Phyllo- and tectoman-  
52 ganates with large tunnel sizes (2×2 and larger; hollandite, romanèchite, todorokite), (2) tec-  
53 tomanganates with small tunnel sizes (2×2 and smaller; cryptomelane, pyrolusite,  
54 ramsdellite), (3) Mn(III)-dominated species (nesosilicates, oxyhydroxides, organic com-  
55 pounds, spinels), (4) Mn(II) species (carbonate, phosphate, and phyllosilicate minerals, ad-  
56 sorbed and organic species), and (5) manganosite. All Mn compounds, except for members of  
57 the manganate group (excluding pyrolusite) and adsorbed Mn(II) species, exhibit unique EX-  
58 AFS spectra that would allow their identification and quantification in mixtures. Therefore,  
59 our results highlight the potential of Mn K-edge EXAFS spectroscopy to assess bulk Mn spe-  
60 ciation in soils and sediments. A complete XAS-based speciation analysis of bulk Mn in envi-  
61 ronmental samples should preferably include the determination of Mn valences following the  
62 ‘Combo’ method of Manceau et al. (2012) (American Mineralogist 97, 816-827), EXAFS  
63 LCF analyses based on principal component and target transformation results, as well as EX-  
64 AFS shell-fit analyses for the validation of LCF results. For this purpose, all 32 XAS refer-  
65 ence spectra are provided in the Supplementary material for further use by the scientific  
66 community.

67

## INTRODUCTION

68 Manganese (Mn) is a redox-sensitive element with a crustal abundance of about 0.1 wt.%  
69 (Yaroshevsky, 2006). It participates in numerous globally important environmental processes  
70 such as photosynthetic oxygen production and oxidative lignin degradation, and serves as an  
71 activator of more than 35 enzymes (Broadley et al., 2012; Burnell, 1988; Jensen et al., 1996;  
72 Keiluweit et al., 2015). The three naturally occurring Mn oxidation states +2, +3, and +4 ac-  
73 count for the large variety of mono- and mixed-valent Mn species in environmental samples,  
74 including oxides and oxyhydroxides (collectively termed (oxyhydr)oxides), carbonates, phos-

75 phates, silicates, organic compounds or Mn species being adsorbed to (in)organic surfaces.  
76 Manganese concentrations in sediments and bedrocks may be as low as 20 mg/kg in quartz  
77 sands and >1,000 mg/kg in basic rocks like basalt and gabbro (Blume et al., 2016; Gilkes and  
78 McKenzie, 1988). Natural background levels of soil Mn range between 40 and 1,000 mg/kg  
79 (Blume et al., 2016), but neither total nor exchangeable Mn in soil is correlated with bedrock  
80 composition, indicative of a high Mn mobility in the Earth's crust (Mortvedt, 2000).

81 The mobility of Mn in soils and sediments depends largely on biological processes  
82 controlling its redox state (Tebo et al., 2005). Since  $\text{Mn}^{2+}$  is more soluble than  $\text{Mn}^{4+}$ , Mn bio-  
83 availability tends to increase with decreasing pH and redox potential (Blume et al., 2016). A  
84 particularly important role in the cycling of Mn in surface environments is attributed to  
85 Mn(III/IV) (oxyhydr)oxides, since their precipitation and dissolution primarily control the  
86 amount of soluble and thus bioavailable  $\text{Mn}^{2+}$  (Martin, 2005; Tebo et al., 2004). These miner-  
87 als exist either as layer or tunnel structures. Layer-type Mn(III/IV) (oxyhydr)oxides ('phyl-  
88 lomanganates') consist of stacked sheets of edge-sharing  $\text{MnO}_6$  octahedra, whereas in  
89 Mn(III/IV) (oxyhydr)oxides with tunnel structure ('tectomanganates')  $\text{MnO}_6$  octahedra form  
90 single, double or triple chains by sharing edges, which are linked together via  $\text{MnO}_6$  corners  
91 to produce tunnels of varying size (McKenzie, 1989). Positive charge deficits created by  $\text{Mn}^{4+}$   
92 site vacancies or the substitution of structural  $\text{Mn}^{3+/4+}$  by cations of lower valence are compen-  
93 sated by exchangeable cations (e.g.,  $\text{H}^+$ ,  $\text{Na}^+$ ,  $\text{K}^+$ ,  $\text{Ca}^{2+}$ ,  $\text{Mg}^{2+}$ , etc.) occupying the tunnel or  
94 interlayer spaces (McKenzie, 1989).

95 Manganate minerals are thought to be primarily formed via fast enzymatic  $\text{Mn}^{2+}$  oxi-  
96 dation by bacteria and fungi (Tebo et al., 2004). Resulting Mn(III/IV) (oxyhydr)oxides are  
97 poorly crystalline phylломanganates structurally akin to  $\text{H}^+$ -birnessite ('acid birnessite') or  $\delta$ -  
98  $\text{MnO}_2$ , and may serve as precursors for more crystalline Mn oxides (e.g., todorokite) and

99 Mn(III) oxyhydroxides (e.g., feitknechtite, manganite) through ageing and/or redox reactions  
100 involving dissolved Mn(II) (Elzinga, 2011; Feng et al., 2010; Miyata et al., 2007).

101 The role of Mn(III/IV) (oxyhydr)oxides as strong oxidants for inorganic and organic  
102 soil and sediment constituents is well documented (Bartlett, 1981; Ehlert et al., 2016; Feng et  
103 al., 2007; Remucal and Ginder-Vogel, 2014; Villinski et al., 2001). Owing to their low point  
104 of zero charge and high specific surface area, biogenic Mn(III/IV) (oxyhydr)oxides show a  
105 high affinity towards heavy metals like Co, Cu, Ni, and Zn, which frequently exceeds that of  
106 Fe(III) (oxyhydr)oxides (O'Reilly and Hochella Jr, 2003; Tebo et al., 2004). As a conse-  
107 quence, soil Mn contained in ferromanganese nodules and concretions is often associated with  
108 these trace metals (Latrille et al., 2001; Liu et al., 2002; Manceau et al., 2003).

109 Despite the ecological importance and omnipresence of Mn in terrestrial surface envi-  
110 ronments, studies targeting the identification and quantification of chemical forms (species) of  
111 Mn are surprisingly rare. Available Mn speciation studies can be grouped into three catego-  
112 ries. Category 1 studies used sequential extraction methods (Habibah et al., 2014;  
113 Kalemkiewicz et al., 2008; Narwall and Singh, 2001; Qiang et al., 1994), which provide val-  
114 uable information on operationally defined Mn fractions. However, poor selectivity of ex-  
115 tractants, Mn redistribution during extractions, and the use of a large variety of non-  
116 standardized extraction procedures severely limit the explanatory power of this speciation  
117 approach (Hass and Fine, 2010; Hlavay et al., 2004; Sutherland and Tack, 2003). Category 2  
118 studies employed X-ray or electron diffraction to identify and/or characterize Mn minerals in  
119 geomaterials. The use of these techniques is hampered by the fact that Mn minerals in soils  
120 and sediments are frequently nanocrystalline and amorphous to X-rays (Chukhrov and  
121 Gorshkov, 1981; Cornu et al., 2005; Latrille et al., 2001; Rhoton et al., 1993; Ross et al.,  
122 1976; Zhang and Karathanasis, 1997). Therefore, these studies almost exclusively focused on  
123 ferromanganese nodules and concretions in soils (Liu et al., 2002; Manceau et al., 2003;

124 Szymański et al., 2014; Taylor et al., 1964; Tokashiki et al., 1986; Uzochukwu and Dixon,  
125 1986) or sediments (Lee and Xu, 2016; Taira et al., 1981). Category 3 studies utilized syn-  
126 chrotron-based Mn K-edge X-ray absorption spectroscopy (XAS) to speciate soil (Frommer et  
127 al., 2011; Hernandez-Soriano et al., 2012; Herndon et al., 2014; Keiluweit et al., 2015;  
128 Manceau et al., 2005) and sediment Mn (Carroll et al., 2002; Friedl et al., 1997; O'Day et al.,  
129 2000). Regardless of the type of Mn species present, high-brilliance synchrotron facilities  
130 provide the capability for non-destructive analysis of oxidation state and average local (<5 Å)  
131 coordination of Mn in environmental samples with Mn concentrations of several hundred mil-  
132 ligrams per kilogram. Previous XAS studies mostly employed either Mn K-edge X-ray ab-  
133 sorption near edge structure (XANES) or micro-focused extended X-ray absorption fine struc-  
134 ture (EXAFS) spectroscopy. The XANES technique is useful to infer the average oxidation  
135 state (AOS) of Mn in soils and sediments based on the shift of the absorption edge towards  
136 higher energies with increasing Mn AOS (Manceau et al., 2012; McKeown and Post, 2001).  
137 Quantitative information on the fractional amounts of Mn<sup>2+</sup>, Mn<sup>3+</sup>, and Mn<sup>4+</sup> and the resulting  
138 Mn AOS in a sample can be obtained by the ‘Combo’ linear combination fit (LCF) analysis  
139 method of Manceau et al. (2012) using a XANES spectra database of well-characterized  
140 monovalent Mn references. The accuracy of this method was estimated to be 0.04 valence  
141 units (v.u.) in the Mn AOS range +3 to +4, which decreased when the proportion of divalent  
142 Mn was greater than 15% (Manceau et al., 2012). Although this state-of-the-art LCF approach  
143 has already been used to analyze the AOS of soil Mn (Herndon et al., 2014; Keiluweit et al.,  
144 2015), its generic applicability has not been validated by other methods available for Mn AOS  
145 quantification.

146 In addition to the determination of Mn oxidation states, Mn K-edge XANES spectra  
147 may in principle be useful for the identification and quantification of distinct Mn species in  
148 unknown samples using LCF analysis (Frommer et al., 2011; Leven et al., 2018; Morales-

149 Pérez et al., 2021). However, limited numbers of fit references, spectral similarity of different  
150 species, and non-unique LCF solutions can severely limit this approach (Gustafsson et al.,  
151 2020; Scheinost et al., 2002).

152 In contrast to XANES analyses, EXAFS spectroscopy has hitherto only rarely been  
153 used for the identification and quantification of Mn species in soils and sediments (Manceau  
154 et al., 2005; Mayanna et al., 2015). EXAFS evaluations of environmental samples typically  
155 include shell-fit and LCF analyses (Ahmad et al., 2019; Scheckel and Ryan, 2004), the latter  
156 often combined with principal component analysis (PCA) and target transformation (TT) test-  
157 ing (Langner et al., 2012; Manceau et al., 2002; Mikutta and Rothwell, 2016; Scheinost et al.,  
158 2002). Decisive for the success of Mn EXAFS LCF analysis is the existence of a comprehen-  
159 sive spectrum library including relevant Mn species potentially occurring in terrestrial envi-  
160 ronments. Several EXAFS studies provide fundamental information on the local Mn coordi-  
161 nation in a range of Mn compounds (Ahmad et al., 2019; Bhattacharya and Elzinga, 2018;  
162 Manceau and Combes, 1988; Manceau et al., 2005; McKeown and Post, 2001; Silvester et al.,  
163 1997; Webb et al., 2005). However, the number of publicly available Mn EXAFS spectra is  
164 neither sufficient for validation of EXAFS parameters previously determined for specific Mn  
165 species, nor for Mn speciation analysis of soils and sediments. Additionally, systematic stud-  
166 ies on spectral uniqueness of Mn compounds are largely missing. Complicating matters fur-  
167 ther, EXAFS data are lacking for various potentially important Mn species such as Mn-  
168 containing silicate and phosphate minerals, organic Mn(II/III) compounds, and adsorbed  
169 Mn(II) species.

170 The main objective of this study was to evaluate how well and to what extent different  
171 Mn species potentially occurring in terrestrial surface environments such as soils and sedi-  
172 ments can be distinguished by Mn K-edge XANES and EXAFS spectroscopy. To this end, we  
173 collected XAS spectra of 32 well-characterized mineral and organic Mn compounds and ana-

174 lyzed these spectra for features and structural information that allow the discrimination of  
175 distinct Mn species (groups). This information is indispensable for the correct analysis and  
176 interpretation of Mn XAS spectra of environmental samples. In addition, we used redox titra-  
177 tions to verify the accuracy of the ‘Combo’ XANES LCF method of Manceau et al. (2012) for  
178 determining the AOS of Mn in geomaterials.

## 179 **MATERIALS AND METHODS**

### 180 **Manganese reference compounds**

181 The 32 Mn reference samples analyzed in this study, 15 natural and 17 synthetic, belong to  
182 seven main groups: (1) Phylломanganates, (2) tectomanganates, (3) oxide minerals without  
183 tunnel or layer structure, (4) Mn(III) oxyhydroxides, (5) carbonate, phosphate, and silicate  
184 minerals, (6) organic Mn(II/III) compounds, and (7) Mn(II) adsorbed to (in)organic materials.  
185 Table 1 lists all reference compounds along with information on, for example, ideal and em-  
186 pirical formulas, structure type where appropriate, Mn content, and XAS spectrum source.

187

188 Natural mineral samples were carefully handpicked using a binocular microscope. The clean-  
189 est looking crystals or parts with least alteration were chosen for further analysis. Synthetic  
190 bixbyite, manganosite, and pyrolusite were purchased as mineral powders. Cryptomelane was  
191 synthesized according to McKenzie (1971),  $\delta$ -MnO<sub>2</sub>, hexagonal acid and triclinic Na-  
192 birnessites following Villalobos et al. (2003), manganite was synthesized using a slightly  
193 modified protocol from Chiu and Hering (2000), and Ba-free romanèchite following Shen et  
194 al. (2005).

195 Manganese(II) adsorption samples were prepared by batch experiments using a natural  
196 85:15-90:10 illite-smectite mineral with R3 ordering from Füzérradvány, Hungary (<2- $\mu$ m  
197 fraction; Dohrmann et al., 2009) and peat from a raised peat bog (Federseemoor) near Bad



198 Buchau, Germany (40-250- $\mu\text{m}$  fraction; Hoffmann et al., 2012) as adsorbents. Experimental  
199 conditions are detailed in the Supplementary material.

200

## 201 **Characterization of Mn reference compounds**

202 **X-ray diffraction.** All available solids were analyzed by powder X-ray diffraction in Bragg-  
203 Brentano geometry using a Bruker AXS D4 Endeavor diffractometer equipped with a second-  
204 ary graphite monochromator ( $\text{CuK}\alpha_{1,2}$  radiation) and a scintillation counter. X-ray diffraction  
205 patterns were collected at room temperature within a  $2\theta$  range of  $5\text{-}110^\circ$  using a measur-  
206 ing time of 4-10 s per  $0.02^\circ$  step (tube settings: 40 kV/40 mA). The identity of all minerals  
207 was confirmed (Figs. S1 and S2). Minor impurities in ramsdellite result from its transition to  
208 pyrolusite. Natural pyrolusite and groutite showed minor manganite impurities. An unknown  
209 reflection was found in the diffractograms of triclinic Na-birnessite and synthetic cryptome-  
210 lane. Remaining additional diffraction peaks in different Mn compounds could be assigned to  
211 non-Mn phases such as calcite in groutite, annite in hendricksite, and quartz in braunite and in  
212 the peat sample. Literature references or powder diffraction file (pdf) numbers used for XRD  
213 evaluation are compiled in Table S1.

214 **Chemical composition.** Twelve natural minerals were prepared as polished and carbon-  
215 coated thin sections. Their chemical composition was determined by electron probe microa-  
216 nalysis (EPMA) using a CAMECA SX100 instrument equipped with five wavelength-  
217 dispersive spectrometers. A focused beam was used with an acceleration voltage of 15 kV and  
218 a beam current of 15 nA for major elements (Al, Cr, K, Mg, Mn, P, Si, Ti) and 100 nA for  
219 minor or trace elements (Ba, Ca, Cl, F, Fe, Na, Sr, Zn). Counting time on element peaks was  
220 10 s for Al, Ba, Cr, K, Mn, Na, Si, 20 s for Ca, Cl, Fe, Mg, P, Sr, Ti, 30 s for Zn, and 50 s for  
221 F. Background counting times were half on-peak counting times. The following standards  
222 were used for calibrations (element, analyzer crystal):  $\text{Fe}_2\text{O}_3$  (Fe, large lithium fluoride

223 (LLIF)), jadeite (Na, thallium acid phthalate (TAP)), kyanite (Al, TAP), Mn<sub>3</sub>O<sub>4</sub> (Mn, LLIF),  
224 orthoclase (K, pentaerythritol (PET)), wollastonite (Si, Ca, TAP and PET, respectively), oli-  
225 vine (Mg, TAP), TiO<sub>2</sub> (Ti, large pentaerythritol (LPET)), Cr<sub>2</sub>O<sub>3</sub> (Cr, LPET), apatite (P, PET),  
226 NaCl (Cl, LPET), ZnS (Zn, LLIF), SrF<sub>2</sub> (F, Sr, TAP and LPET, respectively), BaSO<sub>4</sub> (Ba,  
227 LPET). Results of these analyses are summarized in Table S2. Detection limits for each ele-  
228 ment measured are listed in Table S3.

229 The chemical composition of six synthetic mineral compounds (acid Na-birnessite,  
230 cryptomelane,  $\delta$ -MnO<sub>2</sub>, manganite, Na-birnessite (tricl), romanèchite) was determined by  
231 inductively coupled plasma–optical emission spectrometry (ICP-OES, Agilent 5900 SVDV)  
232 after acid digestion of the samples at 120-140 °C (Table S2). Acid reagents included 69%  
233 HNO<sub>3</sub> (Suprapur<sup>®</sup>, Roth), 37% HCl (p.a., Roth), and, if necessary, 40% HF (p.a., Merck) and  
234 30% H<sub>2</sub>O<sub>2</sub> (Suprapur<sup>®</sup>, Merck). Peat samples were previously combusted at 550 °C overnight  
235 in a ceramic crucible. The digestions are described in the Supplement material, and detection  
236 limits for each element measured can be found in Table S3. The elemental composition of  
237 remaining reference compounds is given as provided by the supplier (synthetic bixbyite,  
238 manganosite, pyrolusite, organic Mn(II/III) Mn compounds) or as stated in the respective pub-  
239 lications (synthetic feiknechtite and todorokite) (Table 1). For references with adsorbed  
240 Mn(II), the Mn content was determined as described in the Supplementary material.

241 Based on chemical composition, empirical mineral formulas (Table 1) were calculated  
242 after normalization to oxygen. Fractional amounts of Mn valences per formula unit were de-  
243 termined by charge-balance calculations (Deer, 1992). Mineral formulas of synthetic Na-  
244 birnessites and  $\delta$ -MnO<sub>2</sub> are those stated in their respective synthesis protocols. Details on em-  
245 pirical formula calculations are presented in the Supplementary material.

246 **Redox titrations.** Redox titrations for the determination of bulk Mn AOS were performed  
247 after Grangeon et al. (2012) using an automated titration system (TitroLine 7800, SI Analyt-

248 ics). Briefly,  $(\text{NH}_4)_2\text{Fe}(\text{SO}_4)_2 \cdot 6\text{H}_2\text{O}$  ('Mohr's salt') was used to reduce  $\text{Mn}^{3+/4+}$  in Mn refer-  
249 ence compounds to dissolved  $\text{Mn}^{2+}$ . The excess reductant ( $\text{Fe}^{2+}$ ) was back-titrated with  
250  $\text{KMnO}_4$  solution and total Mn determined by the re-oxidation of  $\text{Mn}^{2+}$  to  $\text{Mn}^{3+}$ , stabilized by  
251 pyrophosphate ( $\text{P}_2\text{O}_7^{4-}$ ). All measurements were carried out in duplicates or triplicates.

252 **Manganese K-edge XAS.** Bulk Mn K-edge XAS spectra of 26 Mn reference compounds  
253 were collected at beamline 7-3 of the Stanford Synchrotron Radiation Lightsource (SSRL,  
254 Menlo Park, USA), beamline 5-BM-D of the Advanced Photon Source (APS, Argonne,  
255 USA), and beamlines P64 and P65 of PETRA III at the Deutsches Elektronen-Synchrotron  
256 (DESY, Hamburg, Germany). The beamlines were equipped with Si(220) (7-3) and Si(111)  
257 double-crystal monochromators (5-BM-D, P64, P65), which were calibrated by setting the  
258 first-derivative maximum of the K-edge absorption spectrum of elemental Mn to 6,539 eV.  
259 Higher harmonics in the beam were reduced by detuning monochromators by 15-50% and by  
260 harmonic rejection mirrors (P65). In addition, 3- $\mu\text{m}$  Cr filters were used to reduce undesired  
261 fluorescence radiation at beamlines 7-3 and P65. Measurements were performed in both fluo-  
262 rescence and transmission mode utilizing solid-state fluorescence detectors (7- or 30-element  
263 Ge detectors, Vortex SDDs) and ionic chambers, respectively. To avoid beam damage, all  
264 samples were measured at 5-20 K employing He-cryostats or at 77 K (5-BM-D) using a Lin-  
265 cam cell. Details of the sample preparation can be found in the Supplementary material.

266 Spectra were recorded with a maximum energy increment of 5 eV before the edge and  
267 0.2-0.3 eV along the edge. The EXAFS was recorded with a  $k$ -space resolution of  $0.05 \text{ \AA}^{-1}$ .  
268 Five to 20 scans were collected per sample. Spectra of a Mn metal foil were used to correct  
269 for slight energy shifts during sample measurements.

270 Spectral pre-processing, including merging of individual scans, rebinning, and energy  
271 calibration, was conducted in SIXPack (Webb, 2005) or Athena (Ravel and Newville, 2005).  
272 The spectra were further processed in Athena following standard routines. The pre-edge re-

273 gion was fit with a linear function and the post-edge region with a quadratic polynomial. The  
274 edge-step energy,  $E_0$ , was defined as the first maximum of the first XANES derivative. For  
275 background removal the Autobk algorithm was applied. The frequency cut-off parameter,  
276  $R_{\text{bkg}}$ , was set to 0.9-1.1, and the  $k$ -weight for background removal to two or three. A Hanning  
277 window function with a sill width of  $2 \text{ \AA}^{-1}$  was used to Fourier transform the data.

278 In addition to the measured spectra, six XAS spectra were obtained from external  
279 sources (Table 1). Details on their origin and measurement can be found in the respective  
280 publications.

281 **Manganese XAS data analysis.** For the determination of Mn AOS and the fractional amount  
282 of each Mn oxidation state present in the reference compounds, we applied the ‘Combo’ LCF  
283 method of Manceau et al. (2012). For this, normalized XANES spectra were fit using 17 Mn  
284 K-edge XANES spectra of monovalent Mn references available as open source in Manceau et  
285 al. (2012) (deposit item AM-12-037), which were processed as described above. The fits were  
286 performed in Athena over an energy range of -20 to 30 eV ( $E-E_0$ ) by applying a non-  
287 negativity constraint. A single  $E_0$  shift was used for all standards. During the fits, negatively  
288 loaded references were progressively eliminated until only references with positive (or zero)  
289 loadings remained. Each previously deleted reference was then again randomly added and the  
290 fit run again to assure that the global minimum was found using the normalized sum of  
291 squared residuals ( $R$ -factor) as best-fit criterion (Manceau et al., 2012). Eventually, no nega-  
292 tive loadings remained and the total fraction of each Mn oxidation state in the sample ana-  
293 lyzed was calculated as the sum of the individual component fractions (Manceau et al., 2012).

294 Least-squares fits of  $k^3$ -weighted EXAFS spectra of Mn reference compounds were  
295 performed in Artemis (Ravel and Newville, 2005) on a shell-by-shell basis in  $R$ -space ( $R+\Delta R$   
296  $\sim 1-4 \text{ \AA}$ ).  $R$ -space resolution as given by the Rayleigh criterion ( $0.5\pi/(k_{\text{max}}-k_{\text{min}})$ ) was 0.14-  
297 0.20  $\text{\AA}$ , such that atomic shells separated by lower values could not be resolved. Theoretical

298 phase-shift and amplitude functions were calculated with FEFF6 (Ankudinov et al., 1998)  
299 based on crystal-structure information. Partial occupancies due to chemical substitution as  
300 revealed by chemical analyses were accounted for by adding additional atoms into the respec-  
301 tive feff.inp file. For structures containing two or more inequivalent Mn sites (e.g., bixbyite,  
302 hausmannite) aggregated FEFF calculations were used, that is, path lists of individual sites  
303 were automatically merged together and weighted by the fractional population of the site in  
304 the unit cell (Ravel, 2014). The passive amplitude reduction factor,  $S_0^2$ , was fixed to 0.8 dur-  
305 ing optimization. If individually fitted Debye-Waller parameters,  $\sigma^2$ , converged towards simi-  
306 lar values, they were equated in the final fit to reduce the number of fit variables.

307 **Statistics.** The Pearson correlation coefficient was used as a similarity metric for normalized  
308 and first-derivative XANES ( $E = 6,530\text{--}6,600$  eV) as well as  $k^2$ -weighted EXAFS spectra ( $k =$   
309  $2.0\text{--}11.5 \text{ \AA}^{-1}$ ,  $E_0 = 6,563$  eV). Principal component analysis (PCA) was performed on the  $k^2$ -  
310 weighted Mn EXAFS spectra. Suitability of this data for PCA was confirmed by the Kaiser-  
311 Meyer-Olkin (KMO) test in SPSS Statistics (IBM Corp.). In addition, an unsupervised hierar-  
312 chical cluster analysis of the EXAFS spectra was conducted using Ward's clustering algorithm  
313 (Ward, 1963) with squared Euclidean distances as distance measure. Correlation, PC, and  
314 cluster analyses were conducted in Statistica (TIBCO Software Inc.). For linear regression  
315 between XANES- and titration-based Mn AOS, normal distribution of data points, constant  
316 variance of the dependent variable, and independence of residuals were assured by Shapiro-  
317 Wilk and Spearman rank correlation tests as well as Durbin-Watson statistic, respectively,  
318 using SigmaPlot v.14 (Systat Software Inc.).

319

## RESULTS AND DISCUSSION

320 **XANES spectra of Mn references compounds**

321 Figure 1 illustrates absorbance shifts to higher energies with increasing Mn AOS of Mn refer-  
322 ence compounds. Here, a zero-energy value was defined by setting the first maximum of the  
323 first XANES derivative in the pre-edge region (~6,539 eV) to 0 eV. The ordinate represents  
324 the relative energy at which the normalized absorbance XANES signal first reaches 50% of  
325 the edge absorption maximum. Manganese compounds belonging to different Mn AOS  
326 groups are clearly separated, confirming that XANES data allow a general classification of  
327 Mn species with respect to Mn oxidation state.

328 Figure 1

329 Figures 2 and 3 show normalized XANES and corresponding first-derivative spectra of Mn  
330 reference compounds, and Table 2 summarizes primary absorption peaks identified up to  
331 6,570 eV. Phyllo- and tectomanganates with varying amounts of Mn<sup>3+</sup> and Mn<sup>4+</sup> generally  
332 show XANES spectra with broad pre-peaks at 6,541.5-6,543.4 eV, smoothly rising absorption  
333 edges, and maximal absorbances between 6,560.3 and 6,562.5 eV (Fig. 2, Table 2). The simi-  
334 larity of their XANES features suggests that a unique identification of single members in mix-  
335 tures would not generally be possible. However, lithiophorite exhibits a unique edge feature,  
336 leading to two distinct peaks in the first-derivative XANES spectrum at 6,551.5 and 6,557.5  
337 eV. This feature may aid the identification of lithiophorite in mixtures with other phyl-  
338 lomanganates. Among tectomanganates, cryptomelane (2×2 tunnels), hollandite sensu stricto  
339 (s.s.) (2×2 tunnels), romanèchite (2×3 tunnels), and todorokite (3×3 tunnels) possess similar  
340 XANES spectra. In contrast, the first-derivative XANES of pyrolusite (1×1 tunnels) and  
341 ramsdellite (1×2 tunnels) feature characteristic double peaks at ~6,552 and ~6,558 eV (Fig. 2,  
342 Table 2), potentially allowing the identification of tectomanganates with the smallest tunnel  
343 sizes in environmental samples. Differences in XANES spectra observed for natural and syn-

344 thetic tectomanganates (cryptomelanes, pyrolusites, todorokites) reflect the sensitivity of  
345 XANES spectroscopy to variations in mineral composition and/or crystallinity (Fig. 2).

346 Manganese oxides without layer or tunnel structure such as bixbyite (ferric Mn(III)  
347 oxide), hausmannite (Mn(II/III) spinel), and manganosite (Mn(II) oxide) show a greater vari-  
348 ability in their XANES spectra, reflecting different Mn oxidation states and Mn coordination  
349 environments (Fig. 3). While natural and synthetic bixbyites show featureless absorption edg-  
350 es similar to phyllo- and tectomanganates (but distinct differences in their first-derivative  
351 spectra), hausmannite exhibits a prominent shoulder in the absorption edge at ~6,553 eV and  
352 a well-defined absorption maximum at 6,559.1 eV (Fig. 3, Table 2). Similarly, the XANES of  
353 manganosite possesses a modulated absorption edge, a well-defined absorption maximum at  
354 6,555.0 eV, and a distinct post-edge oscillation at 6,568.6 eV (Fig. 3, Table 2). These results  
355 suggest that hausmannite and manganosite can be readily identified in soils and sediments  
356 based on XANES analysis.

357 The Mn<sup>3+</sup>O(OH) polymorphs feitknechtite, groutite, and manganite exhibit similar  
358 XANES features, consisting of smoothly rising absorption edges with two inflection points at  
359 ~6,549 and ~6,556 eV, and absorption maxima located at ~6,560 eV (Fig. 3, Table 2). Varia-  
360 tions among these minerals are subtle, and suggest that groutite and manganite are virtually  
361 indistinguishable by XANES spectroscopy.

362 Carbonate, phosphate, and silicate minerals have unique XANES spectra which also  
363 differ from those of Mn (oxyhydr)oxide minerals. Unsurprisingly, this group displays the  
364 greatest diversity of XANES characteristics. Triplite, a Mn<sup>2+</sup>-containing phosphate, shows a  
365 steep rise in the absorption edge with a non-unique absorption maximum of 6,552.7 eV. In  
366 contrast, rhodochrosite has a pronounced absorption-edge maximum at 6,551.1 eV and a dis-  
367 tinct post-edge absorption maximum at 6,562.4 eV, leading to diagnostic first-derivative  
368 XANES maxima at 6,548.9 and 6,559.9 eV (Fig. 3, Table 2). The two Mn<sup>2+</sup>-bearing triocta-

369 hedral micas hendricksite and masutomilite show similar spectral features with double ab-  
370 sorbance peaks at ~6,552 and ~6,557 eV, which are distinct from all other Mn compounds.  
371 The identification of 2:1 phyllosilicates with structural Mn<sup>2+</sup> may thus be possible in unknown  
372 sample materials. Braunite, a Mn(II/III) nesosilicate, shows a marked step in the absorption  
373 edge and two pronounced peaks in the first-derivative XANES at 6,548.1 and 6,552.9 eV  
374 (Fig. 3, Table 2), comparable to feiknechtite.

375 The XANES of organic Mn compounds differ from each other: While Mn(II) acetate  
376 tetrahydrate has a smoothly rising absorption edge and a broad absorbance maximum similar  
377 to triplite, Mn(II) oxalate dihydrate shows a marked shoulder in the rising part of the edge, a  
378 sharp absorption maximum at 6,553.3 eV, and a characteristic double peak in the first-  
379 derivative XANES at 6,547.0 and 6,551.5 eV (Fig. 3, Table 2). In contrast, Mn(III) acetate  
380 dihydrate exhibits a broad, undulating absorption maximum, which is distinct from all other  
381 Mn references (Fig. 3).

382 Samples with adsorbed Mn(II) (illite, peat) are characterized by smoothly rising ab-  
383 sorption edges, well-defined absorption maxima at ~6,553 eV, and a comparatively feature-  
384 less post-edge absorption (Fig. 3, Table 2). In comparison to the peat samples, Mn(II) ad-  
385 sorbed to illite has a less prominent white-line and two discernable main peaks in the first-  
386 derivative XANES (Fig. 3). The XANES spectra of the peat samples are different from all  
387 other references, and resemble those of Mn(II) citrate, Mn(II) malate, and Mn(II) succinate  
388 (Fernando et al., 2010). This result suggests that Mn(II) complexed by natural organic matter  
389 should be uniquely identifiable in environmental samples. Noteworthy, peat samples prepared  
390 at pH 5 and 7 possess identical XANES spectra, implying that pH had no effect on the coordi-  
391 nation environment of organically bound Mn(II) (Fig. 3).

392 Our results illustrate that Mn compounds differ in absorption-edge energies as related  
393 to Mn AOS, and that several Mn compounds and mineral classes show characteristic inflec-



394 tion points in their XANES spectra. Manganese K-edge XANES features are more pro-  
395 nounced in the respective first-derivative spectra. Since small post-edge normalization errors  
396 do not affect the shape of the derivatives (Manceau et al., 2012), they might be better suited  
397 for fingerprinting and LCF analysis than the respective absorbance spectrum. However,  
398 XANES LCF analyses of natural samples may become biased because XANES spectra of  
399 individual Mn compounds can differ substantially due to variations in chemical composition  
400 and/or crystallinity, as evidenced for bixbyites, cryptomelanes, pyrolusites, and todorokites  
401 (Figs. 2 and 3).

402 Figures 2 and 3, Table 2

#### 403 **Average oxidation state of Mn reference compounds**

404 To obtain information on the Mn AOS and relative fractions of  $\text{Mn}^{2+}$ ,  $\text{Mn}^{3+}$ , and  $\text{Mn}^{4+}$  in the  
405 reference compounds, we used the XANES LCF ‘Combo’ method (Manceau et al., 2012).  
406 The results are tabulated in Table 3. Note, different from other LCF procedures, the ‘Combo’  
407 method does not claim the samples to be mixtures of the standards (Manceau et al., 2012;  
408 Manceau and Nagy, 2012). Therefore, no uncertainties are assigned to individual fractions or  
409 the derived AOS. Manceau et al. (2012) estimated the accuracy of AOS determination by the  
410 ‘Combo’ method to be  $\sim 0.04$  v.u. in phyllo- and tectomanganates (AOS range 3.0-4.0) with a  
411 negligible amount of  $\text{Mn}^{3+}$  in layer structures and less than about 15%  $\text{Mn}^{2+}$ . Based on our fit  
412 results for the synthetic monovalent Mn references manganosite (AOS 2.0), bixbyite (AOS  
413 3.0), and pyrolusite (AOS 4.0), the absolute accuracy of Mn AOS determination using the  
414 ‘Combo’ method was not better than 0.12 v.u. Regression of nominal vs. LCF-derived AOS  
415 for these references resulted in a standard error of the AOS estimate of 0.07 v.u. ( $R^2 = 0.995$ ,  
416  $p < 0.001$ ). This result is consistent with Manceau et al. (2012) showing that increasing pro-  
417 portions of  $\text{Mn}^{2+}$  lead to a decreased accuracy of the LCF ‘Combo’ method.

418 Manganese reference compounds with a nominal Mn AOS of two ( $N = 10$ ) yielded  
419 XANES-derived AOS of 2.0-2.49 ( $\bar{x} = 2.13$ ). In this group, higher AOS determined for hen-  
420 dricksite (2.21), masutomilite (2.49), and Mn(II) adsorbed to illite (2.35) suggest the presence  
421 of up to 50% Mn<sup>3+</sup>. For the mica minerals, this result can be explained by partial oxidation of  
422 Mn<sup>2+</sup> in their octahedral layers. For the illite sample, the result may indicate the formation of  
423 a Mn(III/IV) phase upon partial re-oxidation of adsorbed Mn(II), but this could not be con-  
424 firmed by EXAFS shell-fit results (see below). LCF results of reference compounds with a  
425 nominal AOS of three ( $N = 6$ ) and four ( $N = 4$ ), were largely in agreement with their nominal  
426 AOS ( $\bar{x} = 3.07$  and 3.96, respectively; Table 3).

427 Table 3

428 In order to validate XANES-based Mn AOS, we performed redox titrations for selected refer-  
429 ence compounds with Mn concentrations >1.5 wt.% ( $N = 25$ ). These experiments showed that  
430 the AOS of hausmannite was significantly overestimated by the ‘Combo’ method, most likely  
431 because its pronounced Jahn-Teller distortion of Mn<sup>3+</sup>O<sub>6</sub> octahedra (Jarosch, 1987) was not  
432 adequately reflected by the standard spectra used (Manceau et al., 2012). An unreasonable  
433 titration-based Mn AOS was also observed for triplite (Table 3), which can be attributed to  
434 incomplete reductive dissolution of the sample during the experiment. With the exception of  
435 these two references, the Mn AOS derived from redox titrations were in excellent agreement  
436 with the XANES-based AOS ( $R^2 = 0.988$ ) (Fig. 4). The regression slope was  $0.997 \pm 0.024$  ( $p$   
437  $< 0.0001$ ) and the standard error of estimate 0.08. This result implies that the ‘Combo’ LCF  
438 method, when applied to environmental samples, provides accurate Mn AOS data within ap-  
439 proximately 0.1 v.u. for the entire Mn valence range +2 to +4.

440 Figure 4

441 **EXAFS spectra of Mn references compounds**

442 Figure 5 shows  $k^3$ -weighted Mn K-edge EXAFS spectra and Fourier-transform (FT) magni-  
443 tudes and real parts of one representative of each Mn species group along with the corre-  
444 sponding model fit. The figure exemplifies the diversity of local Mn bonding environments,  
445 which can be expected in natural samples. Corresponding data of the remaining references are  
446 shown in Figures S3 and S4. EXAFS shell-fit parameters of all compounds are summarized in  
447 Table 4. In the following, we detail EXAFS results for each species group, and clarify  
448 (dis)similarities of EXAFS parameters among species (groups).

449 Figure 5, Table 4

450 **Phyllo- and tectomanganates.** Figure 6 illustrates  $k^3$ -weighted Mn K-edge EXAFS spectra of  
451 phyllo- and tectomanganates. Phyllo- and tectomanganates with hexagonal layer symmetry (acid Na-  
452 birnessite,  $\delta$ -MnO<sub>2</sub>, lithiophorite) show very similar EXAFS spectra featuring comparatively  
453 symmetrical oscillations centered at approximately 4.2, 6.7, 9.2, and 10.4 Å<sup>-1</sup>. In contrast, the  
454 spectrum of triclinic birnessite exhibits a split of the small oscillation between 7.9 and 8.2 Å<sup>-1</sup>.  
455 This antinode splitting is attributed to the ordering of structural Mn<sup>3+</sup> in triclinic birnessite  
456 (Ling et al., 2018; Webb et al., 2005) and allows the distinction of phyllo- and tectomanganates with  
457 hexagonal and triclinic layer symmetry. The peak near 8.0 Å<sup>-1</sup> was previously used as a diag-  
458 nostic fingerprint to differentiate between phyllo- and tectomanganates (McKeown and Post,  
459 2001). In this study, however, also 2×3 and 3×3 tectomanganates exhibit a similar spectral  
460 feature in this region (Fig. 6).

461 Tectomanganates can be generally discerned from phyllo- and tectomanganates by a gradually  
462 emerging left-side shoulder of the 6.7-Å<sup>-1</sup> oscillation. This shoulder becomes more intense  
463 with increasing content of corner-sharing octahedra (i.e., smaller tunnel size) and eventually  
464 results in a split oscillation at 6.4 and 6.7 Å<sup>-1</sup>. The relative intensities of this double-feature  
465 are reversed for pyrolusite (1×1 tunnel) as compared to other tectomanganates (Manceau and

466 Combes, 1988) (Fig. 6). Tectomanganates with 2×2 (hollandite s.s., cryptomelane), 1×2  
467 (ramsdellite), and 1×1 (pyrolusite) tunnel structure also possess a pronounced and diagnostic  
468 oscillation at  $\sim 7.4 \text{ \AA}^{-1}$ , which increases and shifts to lower wavenumbers with decreasing tun-  
469 nel size (Fig. 6). Pyrolusites show two distinct troughs at 7.8 and 8.1  $\text{ \AA}^{-1}$ , which are also visi-  
470 ble in attenuated form for ramsdellite, and thus can serve as another diagnostic fingerprint for  
471 tectomanganates with small tunnel sizes. In combination with the pronounced peak near 7.4  
472  $\text{ \AA}^{-1}$  and the unique oscillation at 9.5  $\text{ \AA}^{-1}$ , these results suggest that pyrolusite should be unam-  
473 biguously identifiable in mixtures of phyllo- and tectomanganates.

474 All manganates are additionally characterized by an oscillation at 10.2-10.5  $\text{ \AA}^{-1}$  (Fig.  
475 6). Because this oscillation is not accompanied by a pronounced right-side shoulder in case of  
476 phylломanganates with hexagonal layer structure (Fig. 6), it can aid the identification of tec-  
477 tomanganates, especially those with 1×1, 1×2, and 2×2 tunnel structures, in mixtures with  
478 hexagonal phylломanganates.

479 First O neighbors of Mn in phylломanganates could be modelled with a single shell at  
480 1.90-1.92  $\text{ \AA}$  (Figs. 5 and S3a). Mn-Mn distances of edge-sharing octahedra (Mn-Mn1) were  
481 fit at 2.87-2.92  $\text{ \AA}$ , which accord with values published for hexagonal and pseudo-orthogonal  
482 phylломanganate structures (Webb et al., 2005). For hexagonal birnessite and  $\delta\text{-MnO}_2$ , we  
483 obtained Mn-Mn2 distances of 3.44-3.49  $\text{ \AA}$  (Table 4). These distances are typically assigned  
484 to triple corner-sharing  $\text{Mn}^{3+}$  octahedra at interlayer sites above or below cation vacancies  
485 (Ling et al., 2018; Silvester et al., 1997; Villalobos et al., 2003). Similar to triclinic birnessite,  
486 no Mn-Mn2 contribution was observed for lithiophorite, in agreement with the presence of  
487 exclusively edge-sharing octahedra (Lanson et al., 2000; McKeown and Post, 2001; Silvester  
488 et al., 1997; Villalobos et al., 2003). Two additional O shells were fit at 3.56(3) and 4.14(12)  
489  $\text{ \AA}$ , which accord with the lithiophorite structure published by Wadsley (1952) (Table 4).

490 Tectomanganates (Figs. 5 and S3b) show similar variations in their Mn-O, Mn-Mn1,  
491 and Mn-Mn2 distances as compared to phylломanganates (Table 4). Within this group, first-  
492 shell O neighbors are located at 1.88-1.92 Å, and second- and third-shell Mn neighbors at  
493 2.87-2.90 and 3.43-3.48 Å, respectively. Shell-fit models also included additional O shells at  
494 3.7-3.8 Å (todorokites) and 3.9-4.0 Å (pyrolusites) as well as higher Mn shells at 3.7-3.8 Å  
495 (hollandite s.s.) and 4.4 Å (pyrolusites) (Bolzan et al., 1993; Miura, 1986; Post et al., 2003)  
496 (Table 4). It generally follows that Mn coordination environments in phyllo- and tectomanga-  
497 nates are largely similar, such that interatomic distances up to the third coordination shell pre-  
498 clude any meaningful discrimination of these minerals in environmental samples using EX-  
499 AFS shell-fit analysis.

500 Figure 6

501 **Oxide minerals without layer or tunnel structure.** Bixbyite possesses two inequivalent Mn  
502 sites with an occupancy of 25 and 75% in its unit cell (Geshnizgani, 2014). As a result, two O  
503 subshells at ~1.91 and ~2.24 Å were needed to account for the generally low first-shell ampli-  
504 tudes of natural and synthetic bixbyite (Fig. S3c). The cubic structure of bixbyite is further  
505 characterized by edge- and corner-sharing Mn<sup>3+</sup> octahedra, for which we obtained Mn-Mn  
506 distances of 3.09-3.11 and 3.54-3.57 Å, respectively (Table 4). These distances are consistent  
507 with those published by Longo et al. (2010).

508 The unit cell of hausmannite also contains two inequivalent Mn sites (Jarosch, 1987).  
509 Here, tetrahedral sites are occupied by Mn<sup>2+</sup> and octahedral sites by Mn<sup>3+</sup> cations. For octahe-  
510 drally coordinated Mn<sup>3+</sup>, Mn-O distances were fit with 4.1(3) equatorial O atoms at 1.95(1) Å  
511 and 1.9(3) axial O atoms at 2.27(1) Å, which account for the octahedral Jahn-Teller distortion  
512 approximately parallel to [001] (Jarosch, 1987). A third O shell (~2.01 Å) for tetrahedrally  
513 coordinated Mn<sup>2+</sup> (Longo et al., 2010) was too close to the Mn-O<sub>eq</sub> distance to be included in

514 the model and did not improve the fit ( $F$ -test; Hamilton, 1965). First-shell oxygens are fol-  
515 lowed by two Mn subshells at 2.88(1) and 3.10(0) Å, corresponding to edge-sharing Mn<sup>3+</sup>  
516 octahedra (Longo et al., 2010). The third FT peak of hausmannite (Figs. 5 and S3c) was re-  
517 produced with Mn shells at 3.44(1) and 3.73(1) Å (Table 4). These values are consistent with  
518 tetrahedra-octahedra corner linkages (Longo et al., 2010) and Mn-Mn distances of Mn<sup>2+</sup> tetra-  
519 hedra, respectively (Jarosch, 1987).

520 In contrast to the former two minerals, the first FT peak of cubic manganosite could be  
521 modeled with a single O shell at 2.22(0) Å (Fig. S3c). Analogous to Ressler et al. (1999),  
522 higher coordination shells were fit with Mn neighbors at 3.13(0) Å, indicative of edge-sharing  
523 Mn<sup>2+</sup> octahedra, and third-shell O atoms at 3.84(0) Å (Fig. S3c, Table 4).

524 **Manganese(III) oxyhydroxides.** Minerals of this group are characterized by reduced first-  
525 shell amplitudes typically caused by the broad distribution of Mn-O bond lengths and associ-  
526 ated scattering cancellation effects (Silvester et al., 1997; Webb et al., 2005) (Figs. 5 and  
527 S4a). Consequently, first-shell oxygens in Mn(III) oxyhydroxides were fit with two or three O  
528 subshells. For feitknechtite, we obtained Mn-O distances of 1.91(0) and 2.22(1) Å, for grout-  
529 ite 1.93(1), 2.15(4), and 2.34(2) Å, and for manganite 1.93(0) and 2.28(1) Å (Table 4). Sec-  
530 ond-shell Mn in feitknechtite was fit at 2.83(1) and 2.99(0) Å, respectively, and third-shell  
531 Mn at 3.33(1) Å (Table 4). The latter distance is considerably shorter than the 3.43 Å reported  
532 by Mackle et al. (1993), but more consistent with the presumed sole presence of edge-sharing  
533 Mn<sup>3+</sup> octahedra in feitknechtite. The coordination numbers ( $CNs$ ) of the two Mn1 subshells in  
534 feitknechtite were previously either set to four and two, respectively (Ressler et al., 1999), or  
535 to unity (Mackle et al., 1993). We obtained  $CNs$  of 1.9(3) and 3.8(11) (Table 4), which are in  
536 good agreement with the values used by Ressler et al. (1999).

537 In contrast to the other two polymorphs, first Mn neighbors in groutite could be fit  
538 with a single shell at 2.88(1) Å (Table 4). Higher Mn coordination shells corresponding to

539 edge- and corner-sharing  $\text{Mn}^{3+}$  octahedra occur at 3.38(3) and 3.61(1) Å, respectively (Table  
540 4). These distances are within the error range of values published by Scheinost et al. (2001).  
541 For manganite, we obtained Mn-Mn1 distances of 2.77(1) and 2.98(2) Å, a Mn-Mn2 distance  
542 of 3.69(1), and a Mn-Mn3 distance of 3.83(2) Å (Table 4). The former can be assigned to Mn  
543 atoms in chains of edge-sharing  $\text{Mn}^{3+}$  octahedra and the latter two to corner-sharing octahedra  
544 (Mackle et al., 1993). Even though our Mn-Mn1/2 distances are up to ~0.07 Å longer than  
545 those reported for manganite by Mackle et al. (1993), they fit well with crystallographic data  
546 (Dachs, 1963). Contrary to Mackle et al. (1993), who postulated a similar local Mn coordina-  
547 tion environment in manganite and feitknechtite, our data imply a substantially different Mn  
548 coordination within these minerals.

549 **Carbonate, phosphate, and silicate minerals.** In minerals of this group, atoms other than O  
550 and Mn/Fe contribute to their EXAFS: Al/Si in masutomilite, C in rhodochrosite, P in triplite,  
551 and Zn in hendricksite. To the best of our knowledge, most of these minerals have not previ-  
552 ously been studied by Mn EXAFS spectroscopy. Their spectra and model fits are depicted in  
553 Figs. 5 and S4b. Generally, first-shell O/F neighbors within this mineral group are found at  
554 distances of 1.94-2.55 Å, and were accounted for by one (hendricksite, masutomilite, rhodo-  
555 chrosite), two (triplite) or three subshells (braunite) (Table 4). Braunite shows a very broad  
556 first FT peak with low amplitude (Fig. S4b), which was fit with 2.6(2), 2.1(3), and 0.9(3) O  
557 neighbors at 1.94(1), 2.25(1), and 2.55(3) Å, respectively. Higher shells included 1.9(5) Mn  
558 atoms at 3.17(1) Å, typical of edge-sharing Mn octahedra, and 5.3(18) O atoms at 3.77(2) Å  
559 (Table 4). All parameters agree well with crystallographic data (Ohmann et al., 1998).

560 The first coordination shell of hendricksite was fit with 4.9(9) O atoms at 2.16(1) Å,  
561 implying fairly distorted  $\text{Mn}^{2+}$  octahedra in this mica mineral. Second-shell signals arise from  
562 Mn/Fe and Zn neighbors at 3.14(1) Å, sharing the same atomic position in the unit cell (Rob-  
563 ert, 1985). The CNs of second-shell Mn/Fe and Zn atoms were set to 2.0 and 2.5, respectively,

564 based on chemical analysis (1.04 apfu Mn+Fe and 1.28 apfu Zn in octahedral coordination).  
565 Magnesium was neglected due to its low scattering amplitude, and Ba and Ti atoms due to  
566 their low concentrations (Table 1).

567         Similar to hendricksite, the first coordination shell in masutomilite was reproduced by  
568 4.9(9) O/F atoms at a distance of 2.15(1) Å. The CNs of second-shell Al and Mn, both located  
569 at 3.02(5) Å, were set to 2.5 and 0.4, respectively, based on chemical analysis (1.23 apfu Al  
570 and 0.18 apfu Mn in octahedral coordination). Octahedral-layer Li was not included in the  
571 model due to its low scattering amplitude. Higher shells of masutomilite include four Al/Si  
572 atoms at 3.24(3) Å and four O atoms at 3.47(3) Å (Table 4).

573         For rhodochrosite, the only important Mn carbonate occurring in soils and sediments  
574 (Barreto et al., 2016; Ying et al., 2011), first O neighbors belonging to the CO<sub>3</sub><sup>2-</sup> group were  
575 fit at 2.19(1) Å. These were followed by a C shell at 3.08(2) Å, Mn shells at 3.79(1) and  
576 4.75(1) Å, and O shells at 3.28(1), 4.10(3), and 4.58(1) Å (Table 4). All distances are in  
577 agreement with Friedl et al. (1997), except for the longest Mn-O distance, which is ~0.03 Å  
578 shorter than previously reported.

579         The FT of triplite is dominated by first-shell F/O atoms, followed by two smaller  
580 peaks hosting Fe/Mn and P neighbors (Fig. S4b). First-shell F and O atoms were fit at 2.05(3)  
581 and 2.15(1) Å, respectively, atoms of edge-sharing Fe/Mn octahedra at 2.93(2) Å, and P at-  
582 oms at 3.55(1) Å (Table 4). Chemical analysis suggested 1.6 F and 4.4 O neighbors (0.79 apfu  
583 F and 2.21 apfu O) in the first coordination shell, which is close to theoretical F and O CNs of  
584 two and four, respectively (Waldrop, 1969).

585 **Organic Mn(II/III) compounds.** The local Mn coordination in Mn(II) acetate tetrahydrate,  
586 Mn(II) oxalate dihydrate, and Mn(III) acetate dihydrate has, to our knowledge, not previously  
587 been studied by EXAFS spectroscopy. Their spectra are displayed in Figures 5 and S4c. The  
588 first coordination shell of both Mn(II) compounds was fit with approximately six O atoms at



589 2.18(1) Å. In contrast, two O subshells housing 5.2(5) and 1.5(5) O atoms at 1.93(0) and  
590 2.20(1) Å, respectively, were needed to model the first FT peak of Mn(III) acetate dihydrate  
591 (Table 4). For Mn(II) acetate tetrahydrate, distances of C and Mn shells were fit at 3.19(4)  
592 and 3.40(2) Å, respectively (Table 4). Remarkably, the best fit was obtained with C and Mn  
593 CNs fixed to nominal values of monoclinic Mn(II) acetate dihydrate ( $P2_1/c$ ) (Cheng and  
594 Wang, 1991). The determined Mn-Mn distance is 0.2 Å shorter than expected for single cor-  
595 ner-sharing Mn octahedra present in monoclinic Mn(II) acetate tetrahydrate ( $P2_1/c$ ) (Bertaut  
596 et al., 1974; Tranqui et al., 1977), but is consistent with long edge-sharing octahedral linkages  
597 as in Mn(II) acetate dihydrate (Cheng and Wang, 1991).

598 In Mn(II) oxalate dihydrate, four proximal C atoms are located at 2.95(2) Å, followed  
599 by distant O atoms at 3.93(2) Å. In addition, three multiple-scattering (MS) paths were in-  
600 cluded in the model (Table 4), which significantly improved the fit ( $F$ -test). Our fit results  
601 comply with XRD data for monoclinic Mn(II) oxalate dihydrate ( $C2/c$ ), and demonstrate the  
602 absence of octahedral linkages in Mn(II) oxalate dihydrate (Puzan et al., 2018).

603 In Mn(III) acetate dihydrate, the first coordination shell is followed by four proximal  
604 C atoms at 2.98(2) Å, a substantially shorter distance compared to Mn(II) acetate tetrahydrate  
605 (Table 4). Best fits of higher coordination shells were obtained with two Mn atoms at  
606 3.40(0) Å and two O atoms at 4.37(5) Å (Table 4). Both, distances and CNs comply with  
607 XRD data for monoclinic Mn(III) triacetate dihydrate ( $P2_1/m$ ), in which Mn octahedra are  
608 linked to chains via single corners (Le Bail, 2016; personal communication to the crystallog-  
609 raphy open database (COD), COD ID 3500063).

610 **Adsorbed Mn(II) species.** To the best of our knowledge, molecular-scale information on  
611 Mn(II) adsorbed to clay minerals (illite) and particulate natural organic matter (peat) is cur-  
612 rently not available. Spectra of Mn(II) adsorbed to illite and peat are illustrated in Figures 5  
613 and S4d. The EXAFS of Mn(II) adsorbed to illite is dominated by first-shell signals, housing

614 two O atoms at 1.92(1) Å and four O atoms at 2.16(1) Å (Table 4). Implementation of Al or  
615 Si backscatterers into the model proved unsuccessful, suggesting that hydrated Mn<sup>2+</sup> ions are  
616 primarily adsorbed as outersphere complexes on siloxane surfaces. We found no evidence of a  
617 Mn(III/IV) phase, which could explain the XANES- and titration-derived AOS values >2 ob-  
618 tained for the illite sample (Table 3). This may suggest a similar adsorption mechanism for  
619 Mn<sup>3+</sup> ions or a systematic error in both AOS determination methods, which we consider less  
620 likely.

621 Nearly identical shell-fit results were obtained for Mn(II) adsorbed to peat at pH 5 and  
622 7, showing that pH had a negligible effect on the coordination of organically bound Mn(II).  
623 Both EXAFS were well reproduced with one proximal C atom at 3.20(7) (pH 5) and  
624 3.21(8) Å (pH 7), implying monodentate Mn<sup>2+</sup> complexation by carboxyl groups. Owing to  
625 their low scattering amplitudes, distal C atoms were not included in the model; instead, an  
626 obtuse triangle Mn-C-O MS path was used to reproduce the low FT peaks at ~4.5 Å (Fig. 5,  
627 Table 4). Interestingly, Mn<sup>2+</sup> complexation by particulate organic matter did not lead to Mn<sup>2+</sup>  
628 oxidation under oxic conditions (Table 3).

629 **Comparison of interatomic distances.** When XAS is applied to soils or sediments, over-  
630 absorption can frequently affect the EXAFS amplitude, leading to a bias of fitted CNs. Addi-  
631 tionally, CNs can be influenced by poor crystallinity (i.e., high static disorder) and/or small  
632 particle size relative to crystalline reference compounds (O'Day et al., 2004). As these issues  
633 do not affect the EXAFS frequency, atomic distances are more robust parameters when com-  
634 paring average Mn coordination environments of natural samples.

635 Figure 7 compiles all absorber-single scatter distances determined in this study. The  
636 figure also includes data from various literature sources for comparison (Table S4). Note that  
637 the designation of individual coordination shells is somewhat arbitrary, and for simplicity,  
638 atoms in subshells were considered part of a 'shell'. As evidenced by Friedl et al. (1997), Mn-

639 O bond distances depend on the oxidation state of Mn. In agreement with this, the shortest  
640 Mn-O distances were observed for tectomanganates, and the longest Mn-O distances for  
641 (in)organic Mn(II) species (Fig. 7). In general, average first-shell distances of all reference  
642 compounds can be classified according to their XANES-derived Mn AOS:  $2.14 \pm 0.04$  Å ( $\bar{x} \pm \sigma$ )  
643 for AOS 2.0-2.5 members ( $N = 10$ ),  $2.02 \pm 0.06$  Å for AOS 3.0-3.5 members ( $N = 9$ ), and  
644  $1.90 \pm 0.01$  Å for AOS 3.7-4.0 members ( $N = 13$ ). Differences in average Mn-O/F bond  
645 lengths of AOS groups are significant at the  $p < 0.05$  level (Kruskal-Wallis rank-based ANO-  
646 VA, Dunn's method), except for the AOS 3.0-3.5 and 3.7-4.0 groups. Figure 7 also illustrates  
647 that split shells of first O neighbors are absent in the phyllo- and tectomanganate groups. In  
648 contrast, Mn-O1 subshells or longer Mn-O distances are typical features of all other Mn spe-  
649 cies groups. Likewise, Mn-Mn1 distances of edge-sharing Mn octahedra in phyllo- and tec-  
650 tomanganates ( $2.87$ - $2.92$  Å) are substantially shorter than corresponding (average) Mn-Mn  
651 distances in (1) oxides without layer or tunnel structure ( $3.03$ - $3.13$  Å; bixbyite, hausmannite,  
652 manganosite), (2) members of the phosphate and silicate group ( $2.93$ - $3.17$  Å; braunite, hen-  
653 dricksite, masutomilite, triplite), and (3) organic Mn(II) compounds ( $3.40$  Å; Mn(II) acetate  
654 tetrahydrate). Although Mn-Mn1 distances of phyllo- and tectomanganates are similar to (av-  
655 erage) Mn-Mn1 distances in Mn(III) oxyhydroxides, the need to fit two Mn-Mn1 subshells to  
656 an EXAFS spectrum of an environmental sample, may indicate the presence of feiknechtite  
657 and manganite (or hausmannite) (Fig. 7).

658 Organic Mn(II/III) compounds may possess edge- or corner-sharing  $\text{MnO}_6$  linkages,  
659 whose Mn-Mn distances can overlap with those of manganate and oxyhydroxide minerals,  
660 notably groutite (Fig. 7). In contrast, organically complexed Mn(II) species lack Mn or other  
661 heavy atoms in higher coordination shells. Their Mn-C distances are either significantly  
662 shorter or longer than the Mn-C distance of rhodochrosite ( $3.08(2)$  Å), thus facilitating the

663 distinction between rhodochrosite and organic Mn(II) species in environmental samples  
664 (Fig. 7).

665 Figure 7

666

667

### 668 **Statistical XAS spectrum comparisons**

669 Key to species detection and quantification by means of Mn XAS LCF is spectral dissimilarity.  
670 Therefore, Pearson correlations were used to compare the (dis)similarity of XAS spectra of  
671 all reference compounds. Normalized XANES spectra (6,530-6,600 eV) were highly positively  
672 correlated due to similar overall shape (Fig. S5), complicating a meaningful species identification  
673 and quantification based on LCF analysis of this data without auxiliary information.  
674 Significantly lower spectral correlations for first-derivative XANES spectra (Fig. S6) indicate  
675 much better discriminative power of these data. Here, low and moderate correlations ( $r \leq 0.7$ )  
676 exist between adsorbed Mn(II) species and most other species-group members. The same  
677 holds for carbonate, silicate, and phosphate minerals as well organic Mn(II) compounds (Fig.  
678 S6). This suggests that members of these groups can likely be identified based on their first-  
679 derivative XANES, provided data quality is sufficient. However, high correlations ( $r > 0.8$ )  
680 were still observed between manganates, oxide minerals without layer or tunnel structure, and  
681 Mn(III) oxyhydroxides, making it difficult to identify and quantify individual members of  
682 these species groups in mixtures using first-derivative XANES spectra (Fig. S6). A much better  
683 discriminative power can be achieved on the basis of Mn EXAFS spectra. Figure 8 shows  
684 the Pearson correlation matrix of  $k^2$ -weighted EXAFS spectra ( $k = 2.0-11.5 \text{ \AA}^{-1}$ ,  $E_0 = 6,563$   
685 eV) of all reference compounds. A  $k^2$ -weighting was chosen because environmental studies  
686 usually deal with low-Mn concentration samples that would not allow a higher  $k$ -weighting in

687 LCF analyses without risking excessive spectral noise amplification. However, caution must  
688 be exercised in interpreting these correlation coefficients because strong correlations were  
689 observed for species whose EXAFS spectra differ substantially, for example, pyrolusite and  
690 Ba-free romanèchite ( $r = 0.82$ ) (cf. Fig. 6). It follows that correlation coefficients of less than  
691 approximately 0.8 can be taken as indication of spectral dissimilarity. Using this criterion,  
692 Figure 8 shows that EXAFS spectra of most reference compounds are unique, only exceptions  
693 being spectra of several members of manganates, organic Mn(II/III) compounds, adsorbed  
694 Mn(II) species, and triplite. This result confirms the supreme potential of EXAFS LCF analy-  
695 sis to identify and quantify individual Mn species in environmental samples.

696       Next, we performed a PCA to reduce the dimensionality of the  $k^2$ -weighted Mn K-  
697 edge EXAFS dataset and clarify spectral group membership. Output parameters for the first  
698 ten principal components (PCs) are summarized in Table S5. The number of statistical mean-  
699 ingful PCs based on eigenvalues  $>1$  (Kaiser-Guttman criterion; Guttman, 1954) was five (Ta-  
700 ble S5). These PCs explained 88.6% of the total variance of all Mn EXAFS spectra, suggest-  
701 ing five superordinate variables defining spectral group membership. A loading plot of PC1  
702 vs. PC2, explaining 56.08% and 13.33% of spectral variance, respectively, is illustrated in  
703 Figure 9. Here, PC1 mainly reflects the oxidation state of Mn reference compounds, as mem-  
704 bers of manganates load highly negatively, Mn(II) species positively, and species with pre-  
705 dominantly Mn(III) intermediately and negatively on PC1. Combined, PCA implies that at  
706 least five Mn species (groups) can be distinguished in the entire EXAFS data set, and Figure 9  
707 suggests that the Mn oxidation state plays a major role.

708       To validate the PCA results, an unsupervised tree-clustering analysis was performed  
709 using Ward's method (Ward, 1963). Figure 10 shows the output of the cluster analysis. The  
710 length of the horizontal lines (linkage distances) is proportional to spectral dissimilarity. Like  
711 PCA, hierarchical cluster analysis generally separated Mn(III/IV) phases from Mn(III)- and

712 Mn(II)-containing compounds at a linkage distance of 25-40 (Fig. 10). A division into five  
713 meaningful clusters, as suggested by PCA, is given at a linkage distance of about 18. Here,  
714 cluster one consists of all phyllomanganates and tectomanganates with large tunnel sizes (2×2  
715 and larger) including hollandite s.s. (2×2 tectomanganate). Cluster two comprises tectoman-  
716 ganates with small tunnel sizes (2×2 and smaller). Minerals dominated by Mn(III) are  
717 grouped into cluster three. Cluster four unites all Mn(II) species, and cluster five is exclusive-  
718 ly formed by manganosite. A closer inspection of inner-cluster variability revealed that bixby-  
719 ite, hausmannite, hendricksite, masutomilite, pyrolusite, and rhodochrosite are clearly distinct  
720 within their respective clusters. While EXAFS spectra with a linkage distance >6 show dis-  
721 criminable spectral features, they become virtually indistinguishable at a linkage distance <5  
722 based on direct comparisons. This implies that six of the 32 Mn reference compounds (haus-  
723 mannite, hendricksite, manganosite, masutomilite, Mn(III) acetate dihydrate, rhodochrosite)  
724 are clearly recognizable and quantifiable as individual species when present in mixtures. All  
725 other Mn compounds can at least be reliably assigned to a particular species group.

726 Figures 8-10

## 727 **IMPLICATIONS**

728 Research on Mn oxidation states in soils and sediments is prerequisite to better understand  
729 redox cycling of Mn and its participation in environmental processes. Since accurate Mn AOS  
730 determination in soils and sediments by wet-chemical methods is impossible due to the excess  
731 of other electron donors/acceptors, especially Fe and organic matter, XANES spectroscopy is  
732 currently the only available tool for process-oriented research relying on this key parameter.  
733 By comparing XANES LCF- and redox titration-based AOS results for mono- and multiva-  
734 lent Mn compounds, we found that the XANES LCF ‘Combo’ method of Manceau et al.

735 (2012) provides accurate Mn AOS data within approximately 0.1 v.u. over the entire natural  
736 Mn valence range.

737       Linear combination fitting of XAS spectra is a widely used method for the identifica-  
738 tion and quantification of element species in environmental samples (Hutchison et al., 2001;  
739 Langner et al., 2012; Leven et al., 2018; Mikutta and Rothwell, 2016; Scheckel and Ryan,  
740 2004). This approach requires comprehensive databases with suitable reference spectra  
741 (Gustafsson et al., 2020; Scheinost et al., 2002). While these exist for several key elements  
742 such as Fe (O'Day et al., 2004; Wilke et al., 2001), they are not available for Mn. Therefore,  
743 we provide (energy-calibrated) XAS spectra of 32 Mn compounds, potentially occurring in  
744 soils and sediments, in the Supplementary material. This spectrum library can be used by the  
745 scientific community for Mn species identification and quantification in terrestrial surface  
746 environments.

747       Prerequisite to the application of XAS LCF for species recognition and quantification  
748 is spectral uniqueness (Gustafsson et al., 2020; Scheinost et al., 2002). Our results show that,  
749 compared to EXAFS spectra, normalized and first-derivative Mn K-edge XANES spectra  
750 provide far less discriminative power to distinguish and thus identify individual Mn species in  
751 environmental samples. Owing to high spectral correlations, the use of normalized Mn  
752 XANES spectra for species identification and quantification in LCF analysis of environmental  
753 samples is not recommended without proper justification based on auxiliary species infor-  
754 mation. First-derivative XANES spectra of most analyzed Mn compounds are unique, sug-  
755 gesting that identification and quantification of most Mn species would be possible. However,  
756 members of the manganate and Mn(III)-oxyhydroxide groups are probably indistinguishable  
757 in mixtures using (first-derivative) XANES spectra. Prominent exceptions are pyrolusite,  
758 ramsdellite, and perhaps lithiophorite, which possess unique first-derivative XANES finger-  
759 prints. Nonetheless, the employment of XANES LCF for Mn species identification and quan-

760 tification in natural samples is limited. First, because XANES features are not solely depend-  
761 ent on the Mn oxidation state or structural and electronic factors, but also on energy calibra-  
762 tion and monochromator resolution (Manceau et al., 2012; Manceau et al., 2002). Second,  
763 because XANES spectra are influenced by subtle changes in chemical composition and/or  
764 crystallinity of Mn compounds. Comparisons of XANES and EXAFS spectra of natural and  
765 synthetic Mn compounds (bixbyites, cryptomelanes, pyrolusites, todorokites) document the  
766 robustness of EXAFS spectroscopy to variations in chemistry and/or crystallinity, demonstrat-  
767 ing its superior value for bulk Mn species identification and quantification in natural samples.  
768 Based on PCA and cluster analyses, EXAFS LCF analysis of environmental samples is at  
769 least capable of discriminating the following species groups: (1) phylломanganates and tec-  
770 tomanganates with large tunnel sizes ( $2\times 2$  and larger; hollandite s.s., romanèchite,  
771 todorokite), (2) tectomanganates with small tunnel sizes ( $2\times 2$  and smaller; cryptomelane, py-  
772 rolusite, ramsdellite), (3) Mn(III)-dominated species (nesosilicates, organic compounds, oxy-  
773 hydroxides, spinels), (4) Mn(II) species (carbonate, phosphate, and phyllosilicate minerals,  
774 adsorbed and organic species), and (5) manganosite. Within these conservatively established  
775 species groups, most Mn compounds exhibit unique EXAFS features, which would assist  
776 their identification and quantification in mixtures using EXAFS LCF analysis. Sole excep-  
777 tions are manganate minerals (except for pyrolusite) and adsorbed Mn(II) species whose EX-  
778 AFS are dominated by first-shell O signals. These results highlight the potential of Mn K-  
779 edge EXAFS spectroscopy to quantitatively assess bulk Mn speciation in soils and sediments,  
780 which so far has not been exploited. For speciation analysis of natural samples using Mn K-  
781 edge EXAFS spectroscopy, we recommend stepwise application of PCA-TT and LCF analy-  
782 sis and subsequent validation of LCF results by spectral fingerprinting as well as EXAFS  
783 shell-fitting in order to justify the presence of individual Mn species.



784 In summary, the results of this study provide a comprehensive framework for the anal-  
785 ysis and interpretation of Mn XAS spectra of natural samples and for the evaluation of the  
786 role of Mn in environmental processes. Our spectrum library thus lays the foundation for fur-  
787 ther process-oriented environmental Mn research.

## 788 ACKNOWLEDGEMENTS

789 We are especially grateful to Evert Elzinga, Flora Brocza, Caroline Peacock, and David  
790 McKeown for providing additional XAS spectra and Reiner Dohrmann for the illite reference.  
791 Special thanks go to Julian Feige for the preparation of thin sections and Philip Weigel for  
792 EPMA assistance. Tobias Fußwinkel is thanked for sharing his knowledge on mineral formula  
793 calculation. Furthermore, we are indebted to Jens Gröger-Trampe and Bodo Mieke (LBEG)  
794 for their support during redox titrations. Use of the Stanford Synchrotron Radiation  
795 Lightsource, SLAC National Accelerator Laboratory, was supported by the U.S. Department  
796 of Energy, Office of Science, Office of Basic Energy Sciences under Contract No. DE-AC02-  
797 76SF00515s. Use of the Advanced Photon Source, an Office of Science User Facility operat-  
798 ed for the U.S. Department of Energy (DOE) Office of Science by Argonne National Labora-  
799 tory, was supported by the U.S. DOE under Contract No. DE-AC02-06CH11357. We also  
800 thank PETRA III at DESY for providing us with beamtime. Assistance at synchrotron facili-  
801 ties by Ritimukta Sarangi (SSRL), Qing Ma (APS), and Edmund Welter, Wolfgang Caliebe,  
802 Akhil Tayal, and Vadim Murzin (all DESY) is gratefully acknowledged. This work was fi-  
803 nancially supported by the DFG (project no. 326242261).

## REFERENCES

- 805 Ahmad, A., van der Wal, A., Bhattacharya, P. and van Genuchten, C.M. (2019)  
806 Characteristics of Fe and Mn bearing precipitates generated by Fe(II) and Mn(II) co-  
807 oxidation with O<sub>2</sub>, MnO<sub>4</sub> and HOCl in the presence of groundwater ions. Water Research  
808 161, 505-516.
- 809 Ankudinov, A.L., Ravel, B., Rehr, J.J. and Conradson, S.D. (1998) Real-space multiple-  
810 scattering calculation and interpretation of X-ray-absorption near-edge structure. Physical  
811 Review B 58, 7565.
- 812 Anthony, J.W., Bideaux, R.A., Bladh, K.W. and Nichols, M.C. (2003) Handbook of  
813 Mineralogy. Mineralogical Society of America, Chantilly, VA 20151-1110, USA.
- 814 Barreto, M.B., Mónaco, S.L., Díaz, R., Barreto-Pittol, E., López, L. and Peralba, M.d.C.R.  
815 (2016) Soil organic carbon of mangrove forests (*Rhizophora* and *Avicennia*) of the  
816 Venezuelan Caribbean coast. Organic Geochemistry 100, 51-61.
- 817 Bartlett, R.J. (1981) Nonmicrobial nitrite-to-nitrate transformation in soils. Soil Science  
818 Society of America Journal 45, 1054-1058.
- 819 Bertaut, E., Tran Qui, D., Burlet, P., Thomas, M. and Moreau, J. (1974) Crystal structure of  
820 manganese acetate tetrahydrate. Acta Crystallographica Section B: Structural  
821 Crystallography and Crystal Chemistry 30, 2234-2236.
- 822 Bhattacharya, L. and Elzinga, E.J. (2018) A comparison of the solubility products of layered  
823 Me(II)-Al(III) hydroxides based on sorption studies with Ni(II), Zn(II), Co(II), Fe(II),  
824 and Mn(II). Soil Systems 2, 20.
- 825 Blume, H., Brümmer, G., Fleige, H., Horn, R., Kandeler, E., Kögel-Knabner, I., Kretzschmar,  
826 R., Stahr, K. and Wilke, B. (2016) Scheffer/Schachtschabel Soil Science. Springer: Berlin  
827 Heidelberg, Germany.
- 828 Bolzan, A., Fong, C., Kennedy, B. and Howard, C. (1993) Powder neutron diffraction study  
829 of pyrolusite, β-MnO<sub>2</sub>. Australian Journal of Chemistry 46, 939-944.
- 830 Broadley, M., Brown, P., Cakmak, I., Rengel, Z. and Zhao, F. (2012) Function of nutrients:  
831 micronutrients. Marschner's Mineral Nutrition of Higher Plants (Third Edition), pp. 191-  
832 248. Elsevier.
- 833 Burnell, J.N. (1988) The biochemistry of manganese in plants. In: Robin D. Graham, R.J.H.,  
834 Nicholas C. Uren, Ed., Manganese in Soils and Plants, pp. 125-137, Dordrecht.
- 835 Carroll, S., O'Day, P.A., Esser, B. and Randall, S. (2002) Speciation and fate of trace metals  
836 in estuarine sediments under reduced and oxidized conditions, Seaplane Lagoon,  
837 Alameda Naval Air Station (USA). Geochemical Transactions 3, 81-101.
- 838 Cheng, C.-Y. and Wang, S.-L. (1991) Structure of manganese acetate dihydrate. Acta  
839 Crystallographica Section C: Crystal Structure Communications 47, 1734-1736.
- 840 Chiu, V.Q. and Hering, J.G. (2000) Arsenic adsorption and oxidation at manganite surfaces.  
841 1. Method for simultaneous determination of adsorbed and dissolved arsenic species.  
842 Environmental Science & Technology 34, 2029-2034.
- 843 Chukhrov, F.V. and Gorshkov, A.I. (1981) Iron and manganese oxide minerals in soils. Earth  
844 and Environmental Science Transactions of The Royal Society of Edinburgh 72, 195-  
845 200.
- 846 Cornu, S., Deschatrettes, V., Salvador-Blanes, S., Clozel, B., Hardy, M., Branchut, S. and Le  
847 Forestier, L. (2005) Trace element accumulation in Mn-Fe-oxide nodules of a planosolic  
848 horizon. Geoderma 125, 11-24.
- 849 Dachs, H. (1963) Neutronen- und Röntgenuntersuchungen am Manganit, MnOOH. Zeitschrift  
850 für Kristallographie – Crystalline Materials 118, 303-326.
- 851 Deer, W.A., Robert Andrew Howie, and Jack Zussman (1992) An Introduction to the Rock-  
852 Forming Minerals, 2<sup>nd</sup> ed. Longman, 712, London.

- 853 Dohrmann, R., Rüping, K.B., Kleber, M., Ufer, K. and Jahn, R. (2009) Variation of preferred  
854 orientation in oriented clay mounts as a result of sample preparation and composition.  
855 *Clays and Clay Minerals* 57, 686-694.
- 856 Ehlert, K., Mikutta, C. and Kretzschmar, R. (2014) Impact of birnessite on arsenic and iron  
857 speciation during microbial reduction of arsenic-bearing ferrihydrite. *Environmental*  
858 *Science & Technology* 48, 11320-11329.
- 859 Ehlert, K., Mikutta, C. and Kretzschmar, R. (2016) Effects of manganese oxide on arsenic  
860 reduction and leaching from contaminated floodplain soil. *Environmental Science &*  
861 *Technology* 50, 9251-9261.
- 862 Elzinga, E.J. (2011) Reductive transformation of birnessite by aqueous Mn(II). *Environmental*  
863 *Science & Technology* 45, 6366-6372.
- 864 Feng, Q., Kanoh, H., Miyai, Y. and Ooi, K. (1995) Metal ion extraction/insertion reactions  
865 with todorokite-type manganese oxide in the aqueous phase. *Chemistry of Materials* 7,  
866 1722-1727.
- 867 Feng, X.H., Zhai, L.M., Tan, W.F., Liu, F. and He, J.Z. (2007) Adsorption and redox  
868 reactions of heavy metals on synthesized Mn oxide minerals. *Environmental Pollution*  
869 147, 366-373.
- 870 Feng, X.H., Zhu, M., Ginder-Vogel, M., Ni, C., Parikh, S.J. and Sparks, D.L. (2010)  
871 Formation of nano-crystalline todorokite from biogenic Mn oxides. *Geochimica et*  
872 *Cosmochimica Acta* 74, 3232-3245.
- 873 Fernando, D.R., Mizuno, T., Woodrow, I.E., Baker, A.J.M. and Collins, R.N. (2010)  
874 Characterization of foliar manganese (Mn) in Mn (hyper)accumulators using X-ray  
875 absorption spectroscopy. *New Phytologist* 188, 1014-1027.
- 876 Friedl, G., Wehrli, B. and Manceau, A. (1997) Solid phases in the cycling of manganese in  
877 eutrophic lakes: New insights from EXAFS spectroscopy. *Geochimica et Cosmochimica*  
878 *Acta* 61, 275-290.
- 879 Frommer, J., Voegelin, A., Dittmar, J., Marcus, M.A. and Kretzschmar, R. (2011)  
880 Biogeochemical processes and arsenic enrichment around rice roots in paddy soil:  
881 Results from micro-focused X-ray spectroscopy. *European Journal of Soil Science* 62,  
882 305-317.
- 883 Geshnizgani, E.R. (2014) Low temperature oxidation of VOCs in air by catalytic ozonation,  
884 Pages, University of Saskatchewan.
- 885 Gilkes, R. and McKenzie, R. (1988) Geochemistry and mineralogy of manganese in soils.  
886 *Manganese in Soils and Plants*, pp. 23-35. Springer.
- 887 Grangeon, S., Manceau, A., Guilhermet, J., Gaillot, A.-C., Lanson, M. and Lanson, B. (2012)  
888 Zn sorption modifies dynamically the layer and interlayer structure of vernadite.  
889 *Geochimica et Cosmochimica Acta* 85, 302-313.
- 890 Gustafsson, J.P., Braun, S., Tuyishime, M.J.R., Adediran, G.A., Warrinnier, R. and  
891 Hesterberg, D. (2020) A probabilistic approach to phosphorus speciation of soils using P  
892 K-edge XANES spectroscopy with linear combination fitting. *Soil Systems* 4, 26.
- 893 Guttman, L. (1954) Some necessary conditions for common-factor analysis. *Psychometrika*  
894 19, 149-161.
- 895 Habibah, J., Khairiah, J., Ismail, B. and Kadderi, M. (2014) Manganese speciation in selected  
896 agricultural soils of peninsular Malaysia. *American Journal of Environmental Sciences*  
897 10, 148-156.
- 898 Hamilton, W.C. (1965) Significance tests on the crystallographic R factor. *Acta*  
899 *Crystallographica* 18, 502-510.

- 900 Hass, A. and Fine, P. (2010) Sequential selective extraction procedures for the study of heavy  
901 metals in soils, sediments, and waste materials – a critical review. *Critical Reviews in*  
902 *Environmental Science and Technology* 40, 365-399.
- 903 Hernandez-Soriano, M.C., Degryse, F., Lombi, E. and Smolders, E. (2012) Manganese  
904 toxicity in barley is controlled by solution manganese and soil manganese speciation. *Soil*  
905 *Science Society of America Journal* 76, 399-407.
- 906 Herndon, E.M., Martínez, C.E. and Brantley, S.L. (2014) Spectroscopic (XANES/XRF)  
907 characterization of contaminant manganese cycling in a temperate watershed.  
908 *Biogeochemistry* 121, 505-517.
- 909 Hlavay, J., Prohaska, T., Weisz, M., Wenzel, W.W. and Stingeder, G.J. (2004) Determination  
910 of trace elements bound to soil and sediment fractions (IUPAC Technical Report). *Pure*  
911 *and Applied Chemistry* 76, 415-442.
- 912 Hoffmann, M., Mikutta, C. and Kretzschmar, R. (2012) Bisulfide reaction with natural  
913 organic matter enhances arsenite sorption: Insights from X-ray absorption spectroscopy.  
914 *Environmental Science & Technology* 46, 11788-11797.
- 915 Hutchison, K.J., Hesterberg, D. and Chou, J.W. (2001) Stability of reduced organic sulfur in  
916 humic acid as affected by aeration and pH. *Soil Science Society of America Journal* 65,  
917 704-709.
- 918 Jarosch, D. (1987) Crystal structure refinement and reflectance measurements of hausmannite,  
919  $Mn_3O_4$ . *Mineralogy and Petrology* 37, 15-23.
- 920 Jensen, K.A., Bao, W., Kawai, S., Srebotnik, E. and Hammel, K.E. (1996) Manganese-  
921 dependent cleavage of nonphenolic lignin structures by *Ceriporiopsis subvermispora* in  
922 the absence of lignin peroxidase. *Applied and Environmental Microbiology* 62, 3679-  
923 3686.
- 924 Kalemkiewicz, J., Sitarz-Palczak, E. and Zapała, L. (2008) A study of the chemical forms or  
925 species of manganese found in coal fly ash and soil. *Microchemical Journal* 90, 37-43.
- 926 Keiluweit, M., Nico, P., Harmon, M.E., Mao, J., Pett-Ridge, J. and Kleber, M. (2015) Long-  
927 term litter decomposition controlled by manganese redox cycling. *Proceedings of the*  
928 *National Academy of Sciences* 112, E5253-E5260.
- 929 Langner, P., Mikutta, C. and Kretzschmar, R. (2012) Arsenic sequestration by organic sulphur  
930 in peat. *Nature Geoscience* 5, 66-73.
- 931 Lanson, B., Drits, V.A., Silvester, E. and Manceau, A. (2000) Structure of H-exchanged  
932 hexagonal birnessite and its mechanism of formation from Na-rich monoclinic busserite at  
933 low pH. *American Mineralogist* 85, 826-838.
- 934 Latrille, C., Elsass, F., Van Oort, F. and Denaix, L. (2001) Physical speciation of trace metals  
935 in Fe-Mn concretions from a rendzic lithosol developed on Sinemurian limestones  
936 (France). *Geoderma* 100, 127-146.
- 937 Lee, S. and Xu, H. (2016) XRD and TEM studies on nanophase manganese oxides in  
938 freshwater ferromanganese nodules from Green Bay, Lake Michigan. *Clays and Clay*  
939 *Minerals* 64, 523-536.
- 940 Lefkowitz, J.P., Rouff, A.A. and Elzinga, E.J. (2013) Influence of pH on the reductive  
941 transformation of birnessite by aqueous Mn(II). *Environmental Science & Technology*  
942 47, 10364-10371.
- 943 Leven, A., Vlassopoulos, D., Kanematsu, M., Goin, J. and O'Day, P.A. (2018)  
944 Characterization of manganese oxide amendments for in situ remediation of mercury-  
945 contaminated sediments. *Environmental Science: Processes & Impacts* 20, 1761-1773.
- 946 Ling, F.T., Post, J.E., Heaney, P.J. and Ilton, E.S. (2018) The relationship between Mn  
947 oxidation state and structure in triclinic and hexagonal birnessites. *Chemical Geology*  
948 479, 216-227.

- 949 Liu, F., Colombo, C., Adamo, P., He, J.Z. and Violante, A. (2002) Trace elements in  
950 manganese-iron nodules from a Chinese Alfisol. *Soil Science Society of America Journal*  
951 66, 661-670.
- 952 Longo, A., Liotta, L.F., Carlo, G.D., Giannici, F., Venezia, A.M. and Martorana, A. (2010)  
953 Structure and the metal support interaction of the Au/Mn oxide catalysts. *Chemistry of*  
954 *Materials* 22, 3952-3960.
- 955 Mackle, P., Charnock, J.M., Garner, C.D., Meldrum, F.C. and Mann, S. (1993)  
956 Characterization of the manganese core of reconstituted ferritin by X-ray absorption  
957 spectroscopy. *Journal of the American Chemical Society* 115, 8471-8472.
- 958 Manceau, A. and Combes, J.M. (1988) Structure of Mn and Fe oxides and oxyhydroxides: A  
959 topological approach by EXAFS. *Physics and Chemistry of Minerals* 15, 283-295.
- 960 Manceau, A., Marcus, M.A. and Grangeon, S. (2012) Determination of Mn valence states in  
961 mixed-valent manganates by XANES spectroscopy. *American Mineralogist* 97, 816-827.
- 962 Manceau, A., Marcus, M.A. and Tamura, N. (2002) Quantitative speciation of heavy metals  
963 in soils and sediments by synchrotron X-ray techniques. *Reviews in Mineralogy and*  
964 *Geochemistry* 49, 341-428.
- 965 Manceau, A. and Nagy, K.L. (2012) Quantitative analysis of sulfur functional groups in  
966 natural organic matter by XANES spectroscopy. *Geochimica et Cosmochimica Acta* 99,  
967 206-223.
- 968 Manceau, A., Tamura, N., Celestre, R.S., MacDowell, A.A., Geoffroy, N., Sposito, G. and  
969 Padmore, H.A. (2003) Molecular-scale speciation of Zn and Ni in soil ferromanganese  
970 nodules from loess soils of the Mississippi Basin. *Environmental Science & Technology*  
971 37, 75-80.
- 972 Manceau, A., Tommaseo, C., Rihs, S., Geoffroy, N., Chateigner, D., Schlegel, M., Tisserand,  
973 D., Marcus, M.A., Tamura, N. and Chen, Z.-S. (2005) Natural speciation of Mn, Ni, and  
974 Zn at the micrometer scale in a clayey paddy soil using X-ray fluorescence, absorption,  
975 and diffraction. *Geochimica et Cosmochimica Acta* 69, 4007-4034.
- 976 Marcus, M.A., Westphal, A.J. and Fakra, S.C. (2008) Classification of Fe-bearing species  
977 from K-edge XANES data using two-parameter correlation plots. *Journal of Synchrotron*  
978 *Radiation* 15, 463-468.
- 979 Martin, S.T. (2005) Precipitation and dissolution of iron and manganese oxides. In: Grassian,  
980 V.H., Ed., *Environmental Catalysis*, pp. 61-82. CRC Press, Boca Raton, Florida.
- 981 Mayanna, S., Peacock, C.L., Schäffner, F., Grawunder, A., Merten, D., Kothe, E. and Büchel,  
982 G. (2015) Biogenic precipitation of manganese oxides and enrichment of heavy metals at  
983 acidic soil pH. *Chemical Geology* 402, 6-17.
- 984 McKenzie, R. (1971) The synthesis of birnessite, cryptomelane, and some other oxides and  
985 hydroxides of manganese. *Mineralogical Magazine* 38, 493-502.
- 986 McKenzie, R.M. (1989) Manganese Oxides and Hydroxides. In: Dixon, J.B., Weed, S.B.,  
987 Eds., *Minerals in Soil Environments*, 2<sup>nd</sup> ed., pp. 439-465. Soil Science Society of  
988 America, Madison, Wisconsin.
- 989 McKeown, D.A. and Post, J.E. (2001) Characterization of manganese oxide mineralogy in  
990 rock varnish and dendrites using X-ray absorption spectroscopy. *American Mineralogist*  
991 86, 701-713.
- 992 Mikutta, C. and Rothwell, J.J. (2016) Peat bogs as hotspots for organoarsenical formation and  
993 persistence. *Environmental Science & Technology* 50, 4314-4323.
- 994 Miura, H. (1986) The crystal structure of hollandite. *Mineralogical Journal* 13, 119-129.
- 995 Miyata, N., Tani, Y., Sakata, M. and Iwahori, K. (2007) Microbial manganese oxide  
996 formation and interaction with toxic metal ions. *Journal of Bioscience and*  
997 *Bioengineering* 104, 1-8.

- 998 Morales-Pérez, A., Moreno-Rodríguez, V., Del Rio-Salas, R., Imam, N.G., González-  
999 Méndez, B., Pi-Puig, T., Molina-Freaner, F. and Loredó-Portales, R. (2021) Geochemical  
1000 changes of Mn in contaminated agricultural soils nearby historical mine tailings: Insights  
1001 from XAS, XRD and SEP. *Chemical Geology*.
- 1002 Mortvedt, J.J. (2000) Bioavailability of micronutrients. In: Sumner, M.E., Ed., *Handbook of*  
1003 *Soil Science*, pp. D-71-88. CRC Press, Boca Raton, FL.
- 1004 Narwall, R. and Singh, B. (2001) Solid phase speciation of iron and manganese in alum shale  
1005 soils studied by parallel and sequential extraction. *Communications in soil science and*  
1006 *plant analysis* 32, 331-349.
- 1007 O'Day, P.A., Carroll, S.A., Randall, S., Martinelli, R.E., Anderson, S.L., Jelinski, J. and  
1008 Knezovich, J.P. (2000) Metal speciation and bioavailability in contaminated estuary  
1009 sediments, Alameda Naval Air Station, California. *Environmental Science & Technology*  
1010 34, 3665-3673.
- 1011 O'Reilly, S.E. and Hochella Jr, M.F. (2003) Lead sorption efficiencies of natural and synthetic  
1012 Mn and Fe-oxides. *Geochimica et Cosmochimica Acta* 67, 4471-4487.
- 1013 O'Day, P.A., Rivera, N., Jr., Root, R. and Carroll, S.A. (2004) X-ray absorption spectroscopic  
1014 study of Fe reference compounds for the analysis of natural sediments. *American*  
1015 *Mineralogist* 89, 572-585.
- 1016 Ohmann, S., Abs-Wurmbach, I., Stüßer, N., Sabine, T. and Westerholt, K. (1998) The  
1017 magnetic structure of braunite  $Mn^{2+}Mn^{3+6}O_8/SiO_4$ . *Zeitschrift für Kristallographie –*  
1018 *Crystalline Materials* 213, 19-27.
- 1019 Peacock, C.L. and Moon, E.M. (2012) Oxidative scavenging of thallium by birnessite:  
1020 Explanation for thallium enrichment and stable isotope fractionation in marine  
1021 ferromanganese precipitates. *Geochimica et Cosmochimica Acta* 84, 297-313.
- 1022 Post, J.E., Heaney, P.J. and Hanson, J. (2003) Synchrotron X-ray diffraction study of the  
1023 structure and dehydration behavior of todorokite. *American Mineralogist* 88, 142-150.
- 1024 Puzan, A.N., Baumer, V.N., Lisovytskiy, D.V. and Mateychenko, P.V. (2018) Structure  
1025 disordering and thermal decomposition of manganese oxalate dihydrate,  $MnC_2O_4 \cdot 2H_2O$ .  
1026 *Journal of Solid State Chemistry* 260, 87-94.
- 1027 Qiang, T., Xiao-quan, S. and Zhe-ming, N. (1994) Evaluation of a sequential extraction  
1028 procedure for the fractionation of amorphous iron and manganese oxides and organic  
1029 matter in soils. *Science of the Total Environment* 151, 159-165.
- 1030 Ravel, B. (2014) Path degeneracy and EXAFS analysis of disordered materials. *Journal of*  
1031 *Synchrotron Radiation* 21, 1269-1274.
- 1032 Ravel, B. and Newville, M. (2005) *ATHENA, ARTEMIS, HEPHAESTUS*: Data analysis for X-  
1033 ray absorption spectroscopy using *IFEFFIT*. *Journal of Synchrotron Radiation* 12, 537-  
1034 541.
- 1035 Remucal, C.K. and Ginder-Vogel, M. (2014) A critical review of the reactivity of manganese  
1036 oxides with organic contaminants. *Environmental Science: Processes & Impacts* 16,  
1037 1247-1266.
- 1038 Ressler, T., Brock, S.L., Wong, J. and Suib, S.L. (1999) Multiple-scattering EXAFS analysis  
1039 of tetraalkylammonium manganese oxide colloids. *The Journal of Physical Chemistry B*  
1040 103, 6407-6420.
- 1041 Rhoton, F., Bigham, J. and Schulze, D. (1993) Properties of iron-manganese nodules from a  
1042 sequence of eroded Fragipan soils. *Soil Science Society of America Journal* 57, 1386-  
1043 1392.
- 1044 Ross, S.J., Franzmeier, D.P. and Roth, C.B. (1976) Mineralogy and chemistry of manganese  
1045 oxides in some Indiana doils. *Soil Science Society of America Journal* 40, 137-143.

- 1046 Scheckel, K.G. and Ryan, J.A. (2004) Spectroscopic speciation and quantification of lead in  
1047 phosphate-amended soils. *Journal of Environmental Quality* 33, 1288-1295.
- 1048 Scheinost, A.C., Kretzschmar, R., Pfister, S. and Roberts, D.R. (2002) Combining selective  
1049 sequential extractions, X-ray absorption spectroscopy, and principal component analysis  
1050 for quantitative zinc speciation in soil. *Environmental Science & Technology* 36, 5021-  
1051 5028.
- 1052 Scheinost, A.C., Stanjek, H., Schulze, D.G., Gasser, U. and Sparks, D.L. (2001) Structural  
1053 environment and oxidation state of Mn in goethite-groutite solid-solutions. *American*  
1054 *Mineralogist* 86, 139-146.
- 1055 Shen, X.F., Ding, Y.S., Liu, J., Cai, J., Laubernds, K., Zenger, R.P., Vasiliev, A., Aindow, M.  
1056 and Suib, S.L. (2005) Control of Nanometer-Scale Tunnel Sizes of Porous Manganese  
1057 Oxide Octahedral Molecular Sieve Nanomaterials. *Advanced Materials* 17, 805-809.
- 1058 Silvester, E., Manceau, A. and Drits, V.A. (1997) Structure of synthetic monoclinic Na-rich  
1059 birnessite and hexagonal birnessite: II. Results from chemical studies and EXAFS  
1060 spectroscopy. *American Mineralogist* 82, 962-978.
- 1061 Sutherland, R.A. and Tack, F.M. (2003) Fractionation of Cu, Pb and Zn in certified reference  
1062 soils SRM 2710 and SRM 2711 using the optimized BCR sequential extraction  
1063 procedure. *Advances in Environmental Research* 8, 37-50.
- 1064 Szymański, W., Skiba, M. and Błachowski, A. (2014) Mineralogy of Fe-Mn nodules in  
1065 Albeluvisols in the Carpathian Foothills, Poland. *Geoderma* 217, 102-110.
- 1066 Taira, H., Kitano, Y. and Kaneshima, K. (1981) Terrestrial ferro-manganese nodules formed  
1067 in limestone areas of the Ryukyu Islands Part I Major and minor constituents of terrestrial  
1068 ferro-manganese nodules. *Geochemical Journal* 15, 69-80.
- 1069 Taylor, R., McKenzie, R. and Norrish, K. (1964) The mineralogy and chemistry of  
1070 manganese in some Australian soils. *Soil Research* 2, 235-248.
- 1071 Tebo, B.M., Bargar, J.R., Clement, B.G., Dick, G.J., Murray, K.J., Parker, D., Verity, R. and  
1072 Webb, S.M. (2004) Biogenic manganese oxides: Properties and mechanisms of  
1073 formation. *Annual Review of Earth and Planetary Sciences* 32, 287-328.
- 1074 Tebo, B.M., Johnson, H.A., McCarthy, J.K. and Templeton, A.S. (2005) Geomicrobiology of  
1075 manganese(II) oxidation. *Trends in Microbiology* 13, 421-428.
- 1076 Tokashiki, Y., Dixon, J. and Golden, D. (1986) Manganese oxide analysis in soils by  
1077 combined X-ray diffraction and selective dissolution methods. *Soil Science Society of*  
1078 *America Journal* 50, 1079-1084.
- 1079 Tranqui, D., Burlet, P., Filhol, A. and Thomas, M. (1977) Redetermination by neutron  
1080 diffraction of the structure of manganese acetate tetrahydrate (MAT). *Acta*  
1081 *Crystallographica Section B: Structural Crystallography and Crystal Chemistry* 33, 1357-  
1082 1361.
- 1083 Uzochukwu, G. and Dixon, J. (1986) Manganese oxide minerals in nodules of two soils of  
1084 Texas and Alabama. *Soil Science Society of America Journal* 50, 1358-1363.
- 1085 Villalobos, M., Lanson, B., Manceau, A., Toner, B. and Sposito, G. (2006) Structural model  
1086 for the biogenic Mn oxide produced by *Pseudomonas putida*. *American Mineralogist* 91,  
1087 489-502.
- 1088 Villalobos, M., Toner, B., Bargar, J. and Sposito, G. (2003) Characterization of the  
1089 manganese oxide produced by *Pseudomonas putida* strain MnB1. *Geochimica et*  
1090 *Cosmochimica Acta* 67, 2649-2662.
- 1091 Villinski, J.E., O'Day, P.A., Corley, T.L. and Conklin, M.H. (2001) In situ spectroscopic and  
1092 solution analyses of the reductive dissolution of MnO<sub>2</sub> by Fe(II). *Environmental Science*  
1093 *& Technology* 35, 1157-1163.

- 1094 Wadsley, A. (1952) The structure of lithiophorite, (Al,Li)MnO<sub>2</sub>(OH)<sub>2</sub>. Acta Crystallographica  
1095 5, 676-680.
- 1096 Waldrop, L. (1969) The crystal structure of triplite, (Mn,Fe)<sub>2</sub>FPO<sub>4</sub>. Zeitschrift für  
1097 Kristallographie – Crystalline Materials 130, 1-14.
- 1098 Ward, J.H. (1963) Hierarchical grouping to optimize an objective function. Journal of the  
1099 American Statistical Association 58, 236-244.
- 1100 Webb, S.M. (2005) SIXpack: A graphical user interface for XAS analysis using IFEFFIT.  
1101 Physica Scripta 2005, 1011.
- 1102 Webb, S.M., Tebo, B.M. and Bargar, J.R. (2005) Structural characterization of biogenic Mn  
1103 oxides produced in seawater by the marine *Bacillus sp.* strain SG-1. American  
1104 Mineralogist 90, 1342-1357.
- 1105 Wilke, M., Farges, F., Petit, P.-E., Brown, G.E., Jr. and Martin, F. (2001) Oxidation state and  
1106 coordination of Fe in minerals: An Fe K-XANES spectroscopic study. American  
1107 Mineralogist 86, 714-730.
- 1108 Yaroshevsky, A. (2006) Abundances of chemical elements in the Earth's crust. Geochemistry  
1109 International 44, 48-55.
- 1110 Ying, S.C., Kocar, B.D., Griffis, S.D. and Fendorf, S. (2011) Competitive microbially and Mn  
1111 oxide mediated redox processes controlling arsenic speciation and partitioning.  
1112 Environmental Science & Technology 45, 5572-5579.
- 1113 Zhang, M. and Karathanasis, A. (1997) Characterization of iron-manganese concretions in  
1114 Kentucky Alfisols with perched water tables. Clays and Clay Minerals 45, 428-439.
- 1115
- 1116



1117

## FIGURE CAPTIONS

1118 **Figure 1.** Classification plot of Mn reference compounds. Different XANES-derived Mn  
1119 AOS based on absorption-edge position are shown relative to the first maximum in the first  
1120 XANES derivative at ~6,540 eV (after Marcus et al., 2008). Note that masutomilite and hen-  
1121 dricksite as well as hausmannite and braunite are separated from other members of the low-  
1122 and medium-AOS range. Synthetic pyrolusite shows the highest Mn AOS of 4.0 of all refer-  
1123 ence compounds.

1124

1125 **Figure 2.** Stacked normalized Mn K-edge XANES (left) and corresponding first-derivative  
1126 spectra (right) of phyllo- and tectomanganates. The spectrum numbers match the numbers in  
1127 Table 1: 1 - acid Na-birnessite (hex, syn), 2 -  $\delta$ -MnO<sub>2</sub> (syn), 3 - lithiophorite, 4 - Na-birnessite  
1128 (tricl, syn), 5 - cryptomelane, 6 - cryptomelane (syn), 7 - hollandite s.s., 8 - pyrolusite, 9 -  
1129 pyrolusite (syn), 10 - ramsdellite, 11 - romanèchite, 12 - romanèchite (Ba-free, syn), 13 -  
1130 todorokite, 14 - todorokite (syn).

1131

1132 **Figure 3.** Stacked normalized Mn K-edge XANES (left) and corresponding first-derivative  
1133 spectra (right) of Mn oxide minerals without layer or tunnel structure as well as Mn(III) oxy-  
1134 hydroxides, carbonate, phosphate, and silicate minerals, organic Mn(II/III) compounds, and  
1135 adsorbed Mn(II) species. The spectrum numbers match the numbers in Table 1: 15 - bixbyite,  
1136 16 - bixbyite (syn), 17 - hausmannite, 18 - manganosite, 19 - feitknechtite (syn), 20 - groutite,  
1137 21 - manganite (syn), 22 - braunite, 23 - hendricksite, 24 - masutomilite, 25 - rhodochrosite,  
1138 26 - triplite, 27 - Mn(II) acetate tetrahydrate (syn), 28 - Mn(II) oxalate dihydrate (syn), 29 -  
1139 Mn(III) acetate dihydrate (syn), 30 - Mn(II) ads. illite pH7, 31 - Mn(II) ads. peat pH5, 32 -  
1140 Mn(II) ads. peat pH7.

1141

1142 **Figure 4.** Linear regression (solid line) between average oxidation state (AOS) of Mn ob-  
1143 tained from redox titrations against Mn AOS determined by XANES LCF. Confidence and  
1144 prediction bands (95%) are indicated by dark and light blue color, respectively. Data for  
1145 hausmannite and triplite (out of range) were excluded from analysis.

1146

1147 **Figure 5.** Stacked  $k^3$ -weighted Mn K-edge EXAFS spectra (left) as well as corresponding  
1148 Fourier-transform magnitudes and real parts (right) of selected Mn reference compounds: 1 -  
1149  $\delta$ -MnO<sub>2</sub> (syn), 2 - hollandite s.s., 3 - hausmannite, 4 - feitknechtite, 5 - rhodochrosite, 6 -  
1150 Mn(II) oxalate dihydrate, 7 - Mn(II) ads. peat pH5. Solid lines represent experimental data  
1151 and dotted lines model fits. EXAFS parameters are summarized in Table 4. The fits of other  
1152 Mn compounds are displayed in Figures S3 and S4.

1153

1154 **Figure 6.** Stacked  $k^3$ -weighted Mn K-edge EXAFS spectra of phyllo- and tectomanganates.  
1155 1 - acid Na-birnessite (hex, syn), 2 -  $\delta$ -MnO<sub>2</sub> (syn), 3 - Na-birnessite (tricl, syn), 4 - lithiopho-  
1156 rite, 5 - todorokite, 6 - todorokite (syn), 7 - romanèchite (nat), 8 - romanèchite (Ba-free, syn),  
1157 9 - hollandite s.s., 10 - cryptomelane (nat), 11 - cryptomelane (syn), 12 - ramsdellite, 13 - py-  
1158 rolusite (nat), 14 - pyrolusite (syn). Vertical lines and black arrows indicate important spectral  
1159 features (see text for details).

1160

1161

1162

1163 **Figure 7.** Interatomic distances between Mn and near-neighbor atoms in Mn reference com-  
1164 pounds obtained from this study (colored symbols) and the literature (gray symbols). Litera-  
1165 ture references are listed in Table S4. In masutomilite, first-shell O could also be F and third-  
1166 shell Al could be Si. In triplite and hendricksite, second-shell Mn may also be Fe. Horizontal  
1167 lines separate the seven different Mn species groups (see text for further details).

1168

1169 **Figure 8.** Pearson correlation matrix for  $k^2$ -weighted Mn K-edge EXAFS spectra ( $k = 2.0$ -  
1170  $11.5 \text{ \AA}^{-1}$ ,  $E_0 = 6,563 \text{ eV}$ ) of Mn reference compounds. Only significant correlations ( $p < 0.05$ )  
1171 are reported.

1172

1173 **Figure 9.** Loading plot of the first two PCs obtained from PCA of  $k^2$ -weighted Mn K-edge  
1174 EXAFS spectra ( $k = 2.0$ - $11.5 \text{ \AA}^{-1}$ ,  $E_0 = 6,563 \text{ eV}$ ) of Mn reference compounds. Species are  
1175 colored according to their XANES-derived Mn AOS.

1176

1177 **Figure 10.** Unsupervised tree clustering of  $k^2$ -weighted Mn K-edge EXAFS spectra ( $k = 2.0$ -  
1178  $11.5 \text{ \AA}^{-1}$ ,  $E_0 = 6,563 \text{ eV}$ ) of Mn reference compounds using Ward's method. Five clusters are  
1179 indicated at a linkage distance of 18.

1180

**Table 1.** Manganese reference compounds studied by XAS

No.	Reference	Mineral formula (nominal / empirical) <sup>a</sup>	Remarks	Mn (wt.%) <sup>b</sup>	Spectrum source
<b>Phyllosilicates</b>					
1	Acid Na-birnessite (hex, syn)	$H_{0.06}K_{0.18}(H_2O)_{0.54}Mn^{3+}_{0.08}(H_2O)_{0.24}(Mn^{4+}_{0.88}vac_{0.12})_{\Sigma 1.00}O_2$		54	This study
2	$\delta$ -MnO <sub>2</sub> (syn)	$(Mn^{4+}, Fe^{3+}, Ca, Na)_{\Sigma 1.00}(O, OH)_2 \cdot nH_2O$		49	This study
3	Lithiophorite	$(Al, Li)Mn^{4+}_2O_2(OH)_2 / Al_2LiMn^{4+}_2Mn^{3+}_6(OH)_6$		39 <sup>c</sup>	McKeown and Post (2001)
4	Na-birnessite (tricl, syn)	$Na_{0.26}(Mn^{4+}_{0.74}Mn^{3+}_{0.26})_{\Sigma 1.00}O_2$		55	This study
<b>Tectomanganates</b>					
5	Cryptomelane	$K(Mn^{4+}, Mn^{3+})_8O_{16} / (K_{0.78}Na_{0.06}Si_{0.05}Ca_{0.04}Zn_{0.03}Sr_{0.02})_{\Sigma 0.98}(Mn^{4+}_{6.73}Mn^{3+}_{1.22}Al_{0.06})_{\Sigma 8.01}O_{16}$	2×2 tunnel	57	This study
6	Cryptomelane (syn)	$K(Mn^{4+}, Mn^{3+})_8O_{16} / (K_{0.89}Pb_{0.01})_{0.90}(Mn^{4+}_{6.79}Mn^{3+}_{1.31})_{\Sigma 8.10}O_{16}$	2×2 tunnel	62	This study
7	Hollandite s.s.	$Ba(Mn^{4+}, Mn^{3+})_8O_{16} / (Ba_{0.75}Pb_{0.16})_{0.91}(Mn^{4+}Mn^{3+}Fe)_{\Sigma 8.00}O_{16}$	2×2 tunnel	n.d.	McKeown and Post (2001)
8	Pyrolusite	$\beta\text{-Mn}^{4+}O_2 / (Mn^{4+}_{0.99}Al_{0.01})_{\Sigma 1.00}O_2$	1×1 tunnel	61	This study
9	Pyrolusite (syn)	$\beta\text{-Mn}^{4+}O_2$	1×1 tunnel	61 <sup>c</sup>	This study
10	Ramsdellite	$R\text{-Mn}^{4+}O_2 / (Mn^{4+}_{0.99}Al_{0.01})_{\Sigma 1.00}O_2$	1×2 tunnel	62	This study
11	Romanèchite	$(Ba, H_2O)_2(Mn^{4+}, Mn^{3+})_5O_{10} / Ba_{0.66}(Mn^{4+}_{3.68}Mn^{3+}_{1.32})_{\Sigma 5.00}O_{10} \cdot 1.34H_2O$	2×3 tunnel	50 <sup>c</sup>	McKeown and Post (2001)
12	Romanèchite (Ba-free, syn)	$(Na, H_2O)_2(Mn)_{10}O_{20} / Na_{1.08}(Mn^{4+}_{4.17}Mn^{3+}_{0.74})_{\Sigma 4.91}O_{10} \cdot H_2O$	2×3 tunnel	60	This study
13	Todorokite	$(Mn^{2+}, Ca, Na, K)(Mn^{4+}, Mn^{2+}, Mg)_6O_{12} \cdot 3H_2O / (Mn^{2+}_{0.18}Ca_{0.22}Na_{0.22}Sr_{0.14}K_{0.11}Zn_{0.08}Ba_{0.03}Si_{0.02})_{\Sigma 0.99}(Mn^{4+}_{5.15}Mn^{2+}_{0.62}Mg_{0.23})_{\Sigma 6.00}O_{12} \cdot 3H_2O$	3×3 tunnel	52	This study
14	Todorokite (syn)	$(Mn^{2+}, Ca, Na, K)(Mn^{4+}, Mn^{2+}, Mg)_6O_{12} \cdot 3H_2O / Mn_{6.1}Mg_{0.7}O_{12} \cdot 3H_2O$	3×3 tunnel	56 <sup>c</sup>	Peacock and Moon (2012)
<b>Oxide minerals without layer or tunnel structure</b>					
15	Bixbyite	$(Mn^{3+}, Fe^{3+})_2O_3 / (Mn^{3+}_{1.74}Fe^{3+}_{0.21}Al_{0.05})_{\Sigma 2.00}O_3$		60	This study
16	Bixbyite (syn)	$Mn^{3+}_2O_3$		70 <sup>c</sup>	This study
17	Hausmannite	$(Mn^{2+}, Mn^{3+})_3O_4 / (Mn^{3+}_{1.97}Mn^{2+}_{1.00}Fe^{3+}_{0.02})_{\Sigma 3.00}O_{4.00}$	Spinel	70	This study
18	Manganosite (syn)	$Mn^{2+}O$		77 <sup>c</sup>	This study
<b>Mn(III) oxyhydroxides</b>					
19	Feitknechtite (syn)	$\beta\text{-Mn}^{3+}O(OH)$		62 <sup>c</sup>	Lefkowitz et al. (2013)
20	Groutite	$\alpha\text{-Mn}^{3+}O(OH) / \alpha\text{-}(Mn^{3+}_{0.98}Mg_{0.1})_{\Sigma 0.99}O(OH)$		60	This study
21	Manganite (syn)	$\gamma\text{-Mn}^{3+}O(OH) / \gamma\text{-Mn}^{3+}_{1.00}O(OH)$		66	This study
<b>Carbonate, phosphate, and silicate minerals</b>					
22	Braunite	$Mn^{3+}Mn^{2+}_6O_8SiO_4 / (Mn^{3+}_{6.08}Mn^{2+}_{0.80}Ca_{0.15}Al_{0.01})_{\Sigma 7.04}O_8Si_{0.95}O_4$	Nesosilicate	61	This study
23	Hendricksite	$K(Zn, Mg, Mn^{2+})_3Si_3AlO_{10}(OH)_2 / (K_{0.93}Na_{0.07})_{\Sigma 1.00}(Zn_{1.28}Mg_{0.76}Mn^{2+}_{0.76}Fe^{2+}_{0.28}Ba_{0.01}Ti_{0.01})_{\Sigma 3.10}(Si_{2.83}Al_{1.17})_{\Sigma 4.00}O_{10}(F_{0.03}(OH)_{1.97})_{\Sigma 2.00}$	Trioctahedral mica	8.3	This study
24	Masutomilite	$K(Li, Al, Mn^{2+})_3(Si, Al)_4O_{10}(F, OH)_2 / (K_{0.85}Na_{0.04})_{\Sigma 0.89}(Li_{1.53}Al_{1.23}Mn^{2+}_{0.18})_{\Sigma 2.94}(Si_{3.43}Al_{0.57})_{\Sigma 4.00}O_9.93(F_{2.06}Cl_{0.01})_{\Sigma 2.07}$	Trioctahedral mica	2.4	This study
25	Rhodochrosite	$Mn^{2+}CO_3 / (Mn^{2+}_{0.94}Zn_{0.03}Ca_{0.02}Mg_{0.01})_{\Sigma 1.00}CO_3$	Carbonate	43	This study
26	Triplite	$(Mn^{2+}, Fe^{2+}, Ca, Mg)_2(PO_4)(F, OH) / (Mn^{2+}_{1.10}Fe^{2+}_{0.74}Ca_{0.10}Mg_{0.05})_{\Sigma 2.00}(P_{0.99}O_{3.96})(F_{0.79}(OH)_{0.21})_{\Sigma 1.00}$	Phosphate	27	This study
<b>Organic Mn(II/III) compounds</b>					
27	Mn(II) acetate tetrahydrate (syn)	$Mn^{2+}(CH_3COO)_2 \cdot 4H_2O$		22 <sup>c</sup>	Ehlert et al. (2014)
28	Mn(II) oxalate dihydrate (syn)	$Mn^{2+}C_2O_4 \cdot 2H_2O$		31 <sup>c</sup>	This study
29	Mn(III) acetate dihydrate (syn)	$Mn^{3+}(CH_3COO)_2 \cdot 2H_2O$		20 <sup>c</sup>	This study
<b>Adsorbed Mn(II) species</b>					
30	Mn(II) ads. illite pH7	$K_{0.65}Al_{2.0}(Al_{0.65}Si_{3.35}O_{10})(OH)_2 \cdots Mn^{2+}_x$	Phyllosilicate	0.7	This study
31	Mn(II) ads. peat pH7		Organic sediment	0.9	This study
32	Mn(II) ads. peat pH5		Organic sediment	1.2	This study

<sup>a</sup> Nominal mineral formulas after Anthony et al. (2003). Empirical formulas of birnessites and  $\delta$ -MnO<sub>2</sub> are taken from Villalobos et al. (2003, 2006), those of hollandite, lithiophorite, and romanèchite from McKeown and Post (2001), and the formula of todorokite (syn) from Feng (1995). All other empirical mineral formulas are based on chemical analysis of this study.

<sup>b</sup> Determined by chemical analysis of this study unless stated otherwise. n.d. = not determined.

<sup>c</sup> Calculated from mineral formula (empirical if two formulas are stated). No chemical analysis performed in this study.

**Table 2.** Primary XANES absorption and first-derivative peaks of Mn reference compounds

No.	Reference	Absorption		First derivative				
		1	2	1	2	3	4	5
<b>Phylломanganates</b>								
1	Acid Na-birnessite (hex, syn)	6562.5		6540.5		6553.5	6558.0	6560.0
2	$\delta$ -MnO <sub>2</sub> (syn)	6561.8		6539.8		6552.5	6556.5	
3	Lithiophorite	6560.4		6539.5	6541.7	6551.5	6557.5	
4	Na-birnessite (tricl, syn)	6560.9		6539.7		6549.2	6553.6	6558.2
<b>Tectomanganates</b>								
5	Cryptomelane	6562.0		6540.8		6556.8		
6	Cryptomelane (syn)	6562.0		6540.6		6557.6		
7	Hollandite s.s	6561.2		6540.0	6542.0	6551.5	6556.0	
8	Pyrolusite	6561.0		6541.0		6552.3	6558.2	
9	Pyrolusite (syn)	6560.3		6540.6	6542.2	6552.7	6558.5	
10	Ramsdellite	6560.9		6540.6	6542.4	6552.2	6558.3	
11	Romanèchite	6561.7		6539.8	6541.7	6551.5	6556.5	
12	Romanèchite (Ba-free, syn)	6561.4		6539.8		6550.7	6557.3	
13	Todorokite	6562.1		6540.6		6551.1	6557.8	
14	Todorokite (syn)	6560.4		6538.9		6549.0	6556.2	
<b>Oxide minerals without layer or tunnel structure</b>								
15	Bixbyite	6558.2		6539.4		6547.9	6549.9	6553.4
16	Bixbyite (syn)	6559.5		6539.8		6548.4	6550.7	6553.8
17	Hausmannite	6559.1		6539.8		6546.8	6550.8	6556.8
18	Manganosite (syn)	6555.0	6568.6	6539.8		6544.5	6550.2	6554.0
<b>Mn(III) oxyhydroxides</b>								
19	Feitknechtite (syn)	6559.7		6539.5		6549.2	6555.5	
20	Groutite	6560.4		6539.0		6549.1	6555.1	
21	Manganite (syn)	6560.7		6539.4		6549.3	6556.1	
<b>Carbonate, phosphate, and silicate minerals</b>								
22	Braunite	6556.4		6540.0		6548.1	6553.0	
23	Hendricksite	6551.9	6556.4	6539.0		6546.9	6550.3	6555.3
24	Masutomilite	6552.3	6557.5	6539.3		6546.1	6551.1	6556.3
25	Triplite	6552.7		6540.1		6547.4	6548.1	
26	Rhodochrosite	6551.1	6562.4	6539.4		6548.9	6559.9	
<b>Organic Mn(II/III) compounds</b>								
27	Mn(II) acetate tetrahydrate (syn)	6551.9		6539.4		6548.4	6564.7	
28	Mn(II) oxalate dihydrate (syn)	6553.3		6539.0		6547.0	6551.5	
29	Mn(III) acetate dihydrate (syn)	6560.8		6539.0		6552.0	6557.5	
<b>Adsorbed Mn(II) species</b>								
30	Mn(II) ads. illite pH7	6552.2		6539.1		6547.4	6551.0	
31	Mn(II) ads. peat pH7	6552.8		6539.8		6549.3		
32	Mn(II) ads. peat pH5	6553.1		6539.5		6549.0		

**Table 3.** Nominal, titration-, and XANES-derived bulk Mn AOS of Mn reference compounds, as well as fractional amounts of Mn<sup>2+</sup>, Mn<sup>3+</sup>, and Mn<sup>4+</sup> (normalized to unity) determined from XANES analysis

No.	Reference	AOS <sup>a</sup> (nominal)	AOS <sup>b</sup> (titration)	AOS (XANES)	Mn <sup>2+</sup>	Mn <sup>3+</sup>	Mn <sup>4+</sup>	Fit sum	R-factor <sup>c</sup> (× 10 <sup>5</sup> )
<b>Phylломanganates</b>									
1	Acid Na-birnessite (hex, syn)	3.92	3.94(0)	3.86	0.04	0.05	0.91	0.99	5
2	δ-MnO <sub>2</sub> (syn)	4.00	3.98(2)	3.90	0.01	0.08	0.91	0.99	11
3	Lithiophorite	3.70	n.d.	3.49	0.02	0.47	0.51	0.97	36
4	Na-birnessite (tricl, syn)	3.57	3.69(1)	3.84	0.03	0.10	0.87	0.97	22
<b>Tectomanganates</b>									
5	Cryptomelane	3.88	3.85(1)	3.84	0.04	0.08	0.88	0.99	9
6	Cryptomelane (syn)	3.88	3.88(2)	3.95	0.00	0.05	0.95	1.02	18
7	Hollandite s.s.	3.75	n.d.	3.75	0.08	0.09	0.83	0.96	42
8	Pyrolusite	4.00	4.03(2)	3.98	0.01	0.00	0.99	0.98	31
9	Pyrolusite (syn)	4.00	4.03(0)	4.00	0.00	0.00	1.00	1.00	21
10	Ramsdellite	4.00	4.02(1)	3.98	0.01	0.00	0.99	1.00	9
11	Romanèchite	3.50	n.d.	3.82	0.02	0.14	0.84	0.98	10
12	Romanèchite (Ba-free, syn)	3.84	3.76(1)	3.91	0.03	0.03	0.94	1.04	8
13	Todorokite	3.67	3.77(2)	3.77	0.01	0.21	0.78	1.02	6
14	Todorokite (syn)	3.67	3.70(2)	3.74	0.04	0.17	0.79	0.99	9
<b>Oxide minerals without layer or tunnel structure</b>									
15	Bixbyite	3.00	3.11(3)	3.08	0.16	0.61	0.24	1.00	17
16	Bixbyite (syn)	3.00	3.05	3.07	0.08	0.78	0.15	1.02	10
17	Hausmannite	2.67	2.72(1)	3.35	0.19	0.27	0.54	0.93	32
18	Manganosite (syn)	2.00	2.04(0)	2.12	0.94	0.00	0.06	1.00	118
<b>Mn(III) oxyhydroxides</b>									
19	Feitknechtite (syn)	3.00	n.d.	3.02	0.02	0.93	0.04	0.97	58
20	Groutite	3.00	3.05(1)	3.17	0.03	0.78	0.20	0.99	14
21	Manganite (syn)	3.00	3.07(3)	3.01	0.02	0.96	0.03	1.02	16
<b>Carbonate, phosphate, and silicate minerals</b>									
22	Braunite	2.86	2.98(4)	2.99	0.10	0.80	0.10	0.98	57
23	Hendricksite	2.00	2.32(11)	2.21	0.79	0.21	0.00	0.96	655
24	Masutomilite	2.00	2.41(13)	2.49	0.51	0.49	0.00	0.98	1130
25	Rhodochrosite	2.00	2.06(1)	2.08	0.96	0.00	0.04	0.99	38
26	Triplite	2.00	1.39(5)	2.01	0.99	0.01	0.00	0.99	62
<b>Organic Mn(II/III) compounds</b>									
27	Mn(II) acetate tetrahydrate (syn)	2.00	n.d.	2.00	1.00	0.00	0.00	0.96	45
28	Mn(II) oxalate dihydrate (syn)	2.00	2.04(1)	2.05	0.95	0.05	0.00	1.01	133
29	Mn(III) acetate dihydrate (syn)	3.00	3.00(0)	3.06	0.00	0.94	0.06	1.02	202
<b>Adsorbed Mn(II) species</b>									
30	Mn(II) ads. illite pH7	2.00	2.48	2.35	0.69	0.26	0.05	1.01	11
31	Mn(II) ads. peat pH5	2.00	n.d.	2.00	1.00	0.00	0.00	1.01	218
32	Mn(II) ads. peat pH7	2.00	n.d.	2.00	1.00	0.00	0.00	1.02	280

<sup>a</sup>Based on nominal mineral formulas (cf. Table 1).

<sup>b</sup>Errors are given as standard deviation of triplicate measurements for the last significant figure. n.d. = not determined. Figures without error assignment are based on single measurements due to limited sample availability.

<sup>c</sup>R-factor =  $\sum_i(\text{data}_i - \text{fit}_i)^2 / \sum_i \text{data}_i^2$ .

**Table 4.** EXAFS parameter determined by shell-fitting of  $k^3$ -weighted Mn K-edge EXAFS spectra of Mn reference compounds<sup>a</sup>

No.	Reference	<i>R</i> -factor <sup>b</sup>	$\chi^2_{\nu}$ <sup>b</sup>	<i>N</i> <sub>idp</sub> <sup>c</sup> <i>k</i> -range	<i>N</i> <sub>var</sub> <sup>c</sup> <i>R</i> -range	$\Delta E_0$ (eV) <sup>d</sup>	<i>CN</i> <sup>e</sup> $\sigma^2$ (Å <sup>2</sup> ) <sup>f</sup>	<i>R</i> (Å) <sup>g</sup>	<i>CN</i> $\sigma^2$ (Å <sup>2</sup> )	<i>R</i> (Å)	<i>CN</i> $\sigma^2$ (Å <sup>2</sup> )	<i>R</i> (Å)	<i>CN</i> $\sigma^2$ (Å <sup>2</sup> )	<i>R</i> (Å)	<i>CN</i> $\sigma^2$ (Å <sup>2</sup> )	<i>R</i> (Å)
<b>Phylломanganates</b>																
1	Acid Na-birnessite (hex, syn)	0.005	856	14.4 2.8-13.2	6 1.0-3.2	2.2(6)	O: 6.2(6) 0.0049(3)	1.90(0)	Mn: 5.3(4) 0.0046(1)	2.89(0)	Mn: 1.2(4) 0.0046	3.49(1)				
2	δ-MnO <sub>2</sub> (syn)	0.007	793	16.1 2.9-13.1	6 1.0-3.5	3.0(7)	O: 5.6(6) 0.0042(3)	1.90(0)	Mn: 4.7(3) 0.0044(2)	2.87(0)	Mn: 1.0 0.0044	3.44(2)				
3	Lithiophorite	0.009	74	14.7 3.5-11.3	8 1.0-4.0	-0.8(11)	O: 4.1(5) 0.0022(3)	1.92(1)	Mn: 6.0 0.0067(3)	2.92(1)	O: 4.0 0.0082(38)	3.56(3)	Mn: 4.0 0.0082	4.14(12)		
4	Na-birnessite (tricl, syn)	0.006	781	12.7 2.6-11.8	5 1.0-3.2	6.1(8)	O: 5.3(5) 0.0030(3)	1.92(0)	Mn: 6.8(8) 0.0066(3)	2.89(0)						
<b>Tectomanganates</b>																
5	Cryptomelane	0.008	769	16.2 2.7-13.0	6 1.0-3.5	0.8(7)	O: 5.0(4) 0.0025(3)	1.90(0)	Mn: 3.7(3) 0.0032(2)	2.88(0)	Mn: 4.0(4) 0.0032	3.44(0)				
6	Cryptomelane (syn)	0.016	351	17.8 2.7-13.0	6 1.0-3.5	1.4(10)	O: 5.8(7) 0.0024(7)	1.91(0)	Mn: 3.7(4) 0.0026(4)	2.89(1)	Mn: 4.2(6) 0.0026	3.45(1)				
7	Hollandite	0.006	142	13.6 3.5-11.3	7 1.0-3.8	-0.7(9)	O: 4.3(5) 0.0032(3)	1.91(0)	Mn: 3.6(4) 0.0062(4)	2.91(1)	Mn: 3.5(5) 0.0062	3.48(1)	Mn: 1.9(5) 0.0062	3.75(1)		
8	Pyrolusite	0.013	290	18.28 2.6-12.3	9 1.0-4.0	-5.5(9)	O: 5.6(8) 0.0028(4)	1.88(1)	Mn: 2.1(4) 0.0018(2)	2.87(1)	Mn: 5.6(6) 0.0018	3.43(1)	O: 8.0 0.0102(35)	4.01(5)	Mn: 4.0 0.0102	4.42(4)
9	Pyrolusite (syn)	0.013	53	23.0 2.7- 4.2	9 1.0-4.2	-5.3(7)	O: 5.6(6) 0.0023(3)	1.88(0)	Mn: 1.9(2) 0.0020(2)	2.88(1)	Mn: 7.1(6) 0.0020	3.43(0)	O: 8.0 0.0030(8)	3.93(2)	Mn: 4.0 0.0030	4.41(1)
10	Ramsdellite	0.006	70	69.3 2.7-13.8	7 1.0-3.6	-6.2(6)	O: 5.6(4) 0.0026(2)	1.89(0)	Mn: 3.2(4) 0.0026(2)	2.88(0)	Mn: 3.8(5) 0.0010(2)	3.43(0)				
11	Romanèchite	0.005	309	10.2 2.8-10.2	6 1.0-3.2	-2.9(10)	O: 4.7(9) 0.0025(4)	1.90(1)	Mn: 4.6(18) 0.0077(6)	2.90(1)	Mn: 2.8(13) 0.0077	3.47(2)				
12	Romanèchite (Ba-free, syn)	0.013	1548	14.5 2.9-11.8	6 1.0-3.6	-2.5(10)	O: 5.7(8) 0.0035(4)	1.90(1)	Mn: 4.4(8) 0.0044(4)	2.88(1)	Mn: 2.4(7) 0.0044	3.44(1)				
13	Todorokite	0.011	1593	18.5 2.6-13.9	9 1.0-3.6	0.4(8)	O: 5.3(5) 0.0032(3)	1.92(0)	Mn: 4.2(7) 0.0049(3)	2.87(0)	Mn: 2.7 0.0027(10)	3.43(1)	O: 6.0 0.0024(21)	3.71(3)		
14	Todorokite (syn)	0.011	834	18.3 2.7-13.9	9 1.0-3.6	-2.1(9)	O: 4.7(4) 0.0033(3)	1.92(0)	Mn: 3.8(8) 0.0055(4)	2.88(1)	Mn: 2.7 0.0069(19)	3.44(2)	O: 6.0 0.0072(43)	3.72(7)		
<b>Oxide minerals without layer or tunnel structure</b>																
15	Bixbyite <sup>h</sup>	0.011	667	14.2 2.6-11.0	5 1.0 - 3.7	-4.3(12)	O1: 4.0(5) 0.0070(6) O2: 1.7(4) 0.0070	1.92(1) 2.24(1)	Mn: 5.2(10) 0.0053(3)	3.11(1)	Mn: 6.0 0.0118(13)	3.57(1)				
16	Bixbyite (syn) <sup>h</sup>	0.020	204	15.9 2.7-12.1	5 1.0-3.7	-6.8(13)	O1: 4.0(6) 0.0059(7) O2: 1.3(6) 0.0059	1.90(1) 2.23(1)	Mn: 5.1(12) 0.0057(4)	3.09(1)	Mn: 6.0 0.0086(9)	3.54(1)				
17	Hausmannite	0.002	66	16.8 2.9-11.8	10 1.0-4.0	0.4(11)	O1: 4.1(3) 0.0071(3) O2: 1.9(3) 0.0071	1.95(1) 2.27(1)	Mn1: 1.3(1) 0.0028(5) Mn2: 2.7(2) 0.0028	2.88(1) 3.10(0)	Mn: 8.1(8) 0.0082	3.44(1)	Mn: 7.7(7) 0.0082(3)	3.73(1)		

**Table 4.** (continued)

No.	Reference	<i>R</i> -factor <sup>b</sup>	$\chi_v^{2b}$	<i>N</i> <sub>idp</sub> <sup>c</sup> <i>k</i> -range	<i>N</i> <sub>var</sub> <sup>c</sup> <i>R</i> -range	$\Delta E_0$ (eV) <sup>d</sup>	<i>CN</i> <sup>e</sup> $\sigma^2$ (Å <sup>2</sup> ) <sup>f</sup>	<i>R</i> (Å) <sup>g</sup>	<i>CN</i> $\sigma^2$ (Å <sup>2</sup> )	<i>R</i> (Å)	<i>CN</i> $\sigma^2$ (Å <sup>2</sup> )	<i>R</i> (Å)	<i>CN</i> $\sigma^2$ (Å <sup>2</sup> )	<i>R</i> (Å)	<i>CN</i> $\sigma^2$ (Å <sup>2</sup> )	<i>R</i> (Å)
<b>Oxide minerals without layer or tunnel structure</b>																
18	Manganosite (syn) <sup>h</sup>	0.010	29	21.8 2.3-13.6	5 1.0-3.6	-2.8(6)	O: 5.8(10) 0.0063(9)	2.22(0)	Mn: 12.0 0.0048(2)	3.13(0)	O: 8.0 0.0164(92)	3.84(0)				
<b>Mn(III) oxyhydroxides</b>																
19	Feitknechtite (syn)	0.002	8	14.2 2.7-11.1	10 1.0-3.7	0.3(7)	O1: 4.0(2) 0.0052(1) O2: 2.0(2) 0.0052	1.91(0) 2.22(1)	Mn1: 1.9(3) 0.0074(4) Mn2: 3.8(11) 0.0074	2.83(1) 2.99(0)	Mn: 4.0 0.0141(1)	3.33(1)	O: 8.0 0.0141	3.60(2)		
20	Groutite	0.008	113	19.1 2.8-13.7	12 1.0-3.8	3.6(11)	O1: 4.2(4) 0.0040(4) O2: 0.9(4) 0.0040 O3: 1.4(3) 0.0040	1.93(1) 2.15(4) 2.34(2)	Mn: 2.1(4) 0.0028(3)	2.88(1)	Mn: 2.0 0.0115(36)	3.38(3)	Mn: 4.0 0.0035(7) O: 8.0 0.0035	3.61(1) 3.77(2)		
21	Manganite (syn)	0.005	214	16.2 2.8-12.4	11 1.1-3.8	1.7(9)	O1: 4.7(4) 0.0062(3) O2: 2.0(3) 0.0062	1.93(0) 2.28(1)	Mn1: 1.0(1) 0.0021(6) Mn2: 1.0(1) 0.0021	2.77(1) 2.98(2)	O: 8.4(18) 0.0062 Mn: 4.0 0.0075(18)	3.61(2) 3.69(1)	Mn: 4.0 0.0075(14)	3.83(2)		
<b>Carbonate, phosphate, and silicate minerals</b>																
22	Braunite	0.011	26	14.9 2.9-11.4	8 1.0-3.8	5.4(10)	O1: 2.6(2) 0.0045(5) O2: 2.1(3) 0.0045 O3: 0.9(3) 0.0045	1.94(1) 2.25(1) 2.55(3)	Mn: 1.9(5) 0.0038(5)	3.17(1)	O: 5.3(18) 0.0063	3.77(2)				
23	Hendricksite	0.017	22	12.1 2.6-11.4	5 1.1-3.3	3.9(13)	O: 4.9(9) 0.0042(8)	2.16(1)	Mn/Fe: 2.0 0.0037(4) Zn: 2.5 0.0037	3.14(1) 3.14						
24	Masutomilite	0.022	52	12.1 2.1-10.5	6 1.0-3.3	4.2(15)	O/F: 4.9(7) 0.0027(1)	2.15(1)	Al: 2.5 0.0100 Mn: 0.4 0.0100	3.02(5) 3.02	Al/Si: 4.0 0.0100	3.24(3)	O: 4.0 0.0100	3.47(3)		
25	Rhodochrosite	0.012	42	21.7 2.2-11.5	12 1.1-4.8	2.7(9)	O: 6.3(8) 0.0050(5)	2.19(1)	C: 6.0 0.0034	3.08(2)	O: 6.0 0.0033(14)	3.28(1)	Mn: 6.0 0.0048	3.79(1)	O1: 6.0 0.0048(4) O2: 4.0 0.0048 Mn: 6.0 0.0032(1)	4.10(3) 4.58(1) 4.75(1)
26	Triplite	0.008	91	12.4 2.3-10.6	7 1.0-3.4	3.6(8)	F: 1.6 0.0067 O: 4.4 0.0067(1)	2.05(3) 2.15(1)	Mn/Fe: 1.0(4) 0.0073(13)	2.93(2)	P: 2.8(7) 0.0073	3.55(1)				

**Table 4. (continued)**

No.	Reference	$R$ -factor <sup>b</sup>	$\chi_v^{2b}$	$N_{\text{idp}}^c$ $k$ -range	$N_{\text{var}}^c$ $R$ -range	$\Delta E_0$ (eV) <sup>d</sup>	$CN^e$ $\sigma^2$ (Å <sup>2</sup> ) <sup>f</sup>	$R$ (Å) <sup>g</sup>	$CN$ $\sigma^2$ (Å <sup>2</sup> )	$R$ (Å)	$CN$ $\sigma^2$ (Å <sup>2</sup> )	$R$ (Å)	$CN$ $\sigma^2$ (Å <sup>2</sup> )	$R$ (Å)	$CN$ $\sigma^2$ (Å <sup>2</sup> )	$R$ (Å)
<b>Organic Mn(II/III) compounds</b>																
27	Mn(II) acetate tetrahydrate (syn)	0.015	175	13.2 2.3-11.1	6.0 1.0-3.4	2.1(10)	O: 5.9(7) 0.0045(0)	2.18(1)	C: 5.2 0.0112(62)	3.19(4)	Mn: 1.6 0.0060(20)	3.40(2)				
28	Mn(II) oxalate dihydrate (syn)	0.029	476	19.0 2.8-12.3	8.0 1.0-4.2	6.9(9)	O: 6.5(6) 0.0041(4)	2.18(1)	C: 4.0 0.0041	2.95(2)	O-C <sup>i</sup> : 8.0 0.0062	3.11(12)	O: 6.0 0.0040	3.93(2)	C-O-C <sup>i</sup> : 4.0 0.0083	4.08(4)
29	Mn(III) acetate dihydrate (syn)	0.013	703	24.2 2.7-13.7	9 0.9-4.4	5.7(8)	O1: 5.2(5) 0.0041(0) O2: 1.5(5) 0.0041	1.93(0) 2.20(1)	C: 4.0 0.0077(24)	2.98(2)	Mn: 2.0 0.0014(3)	3.40(0)	O: 2.0 0.0068(40)	4.37(5)		
<b>Adsorbed Mn(II) species</b>																
30	Mn(II) ads. illite pH7	0.005	5	9.9 2.5-10.5	5 1.0-3.0	-2.4(9)	O1: 2.0 0.0123(18) O2: 4.0 0.0123	1.92(1) 2.16(1)								
31	Mn(II) ads. peat pH5	0.016	540	14.4 2.0-10.5	5 1.3-4.0	3.3(9)	O: 6.0 0.0057(0)	2.18(1)	C: 1.0 0.0057	3.20(7)	C-O <sup>i</sup> : 8.0 0.0086	4.48(5)				
32	Mn(II) ads. peat pH7	0.017	266	14.4 2.0-10.5	5 1.3-4.0	3.4(10)	O: 6.0 0.0051(5)	2.18(1)	C: 1.0 0.0051	3.21(8)	C-O <sup>i</sup> : 8.0 0.0077	4.49(5)				

<sup>a</sup>The amplitude reduction factor,  $S_0^2$ , was set to 0.8 for all fits. Parameter uncertainties are given in parenthesis for the last significant figure.

<sup>b</sup> $R$ -factor =  $\sum_i(\text{data}_i - \text{fit}_i)^2 / \sum_i \text{data}_i^2$  and reduced  $\chi^2 = (N_{\text{idp}}/N_{\text{pts}}) \sum_i ((\text{data}_i - \text{fit}_i)/\epsilon_i)^2 / (N_{\text{idp}} - N_{\text{var}})$ , where  $N_{\text{idp}}$  is the number of independent data points in the model fit,  $N_{\text{pts}}$  the total number of data points,  $N_{\text{var}}$  the number of fit variables (with all CNs set in the final fit), and  $\epsilon_i$  is the uncertainty of the  $i^{\text{th}}$  data point.

<sup>c</sup>Number of independent points and fit variables in final fit, respectively.

<sup>d</sup>Energy-shift parameter.

<sup>e</sup>Coordination number (path degeneracy). Coordination numbers with assigned errors were fit individually and subsequently set in the final fit.

<sup>f</sup>Debye-Waller parameter. If no uncertainties are indicated, parameters were constrained.

<sup>g</sup>Mean half path length.

<sup>h</sup>A volumetric lattice expansion parameter was used to calculate atomic distances in bixbyites and manganosite (cubic crystal system).

<sup>i</sup>Multiple-scattering (MS) path. For Mn(II) oxalate dihydrate, the Debye-Waller parameter of the Mn-O-C obtuse triangle MS path was defined as  $\sigma^2(\text{Mn-O1}) + 0.5\sigma^2(\text{Mn-C})$ ; MS2 (Mn-C-O-C) and MS3 (Mn-C-O) are forward triangle MS paths. Their Debye-Waller parameters were defined as  $\sigma^2(\text{Mn-C}) + \sigma^2(\text{Mn-O1})$  and  $\sigma^2(\text{Mn-C}) + 0.5\sigma^2(\text{Mn-O1})$ , respectively. For Mn(II) adsorbed to peat, the Debye-Waller parameter of the obtuse triangle MS path was defined as  $1.5\sigma^2(\text{Mn-O})$ .



Figure 1

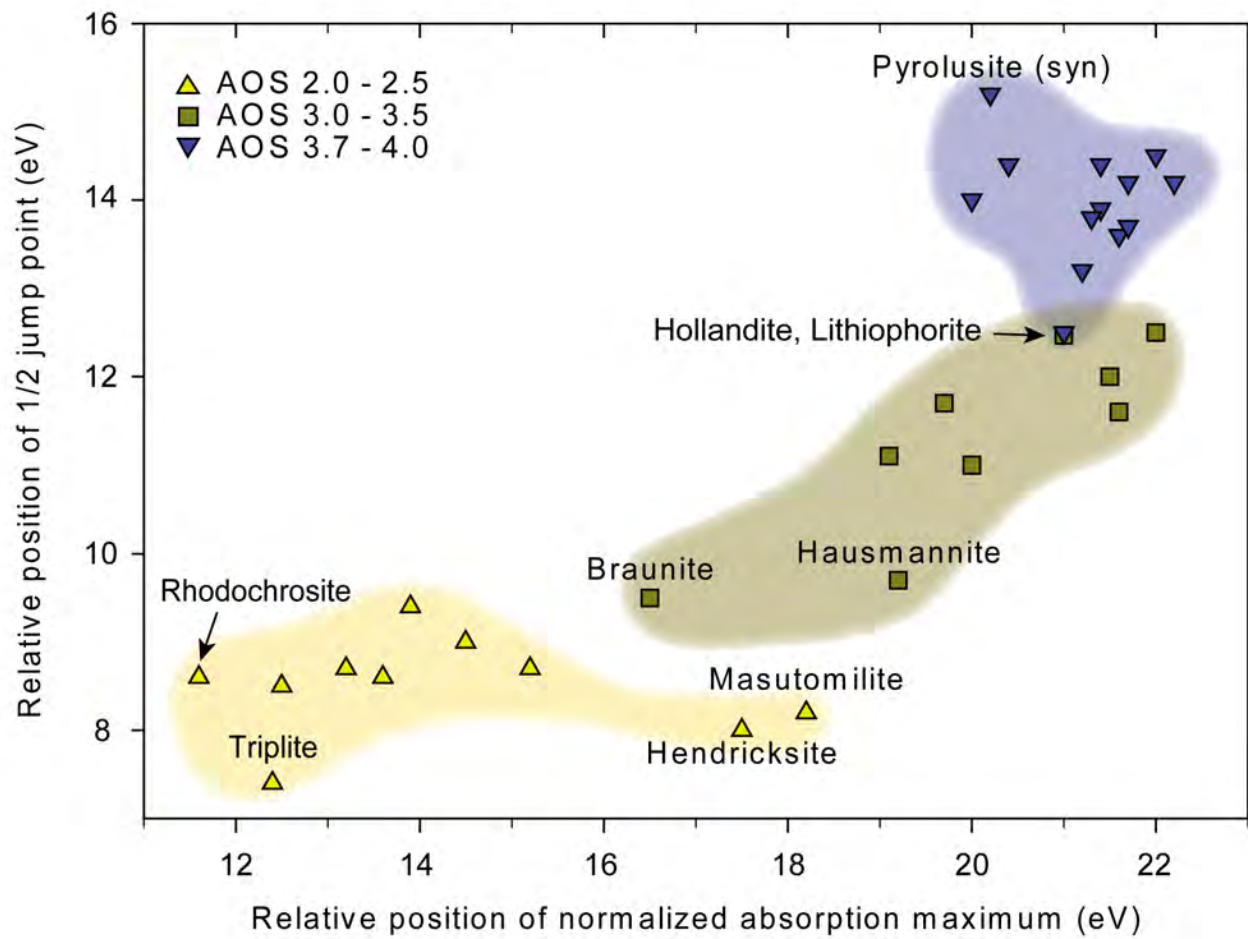


Figure 2

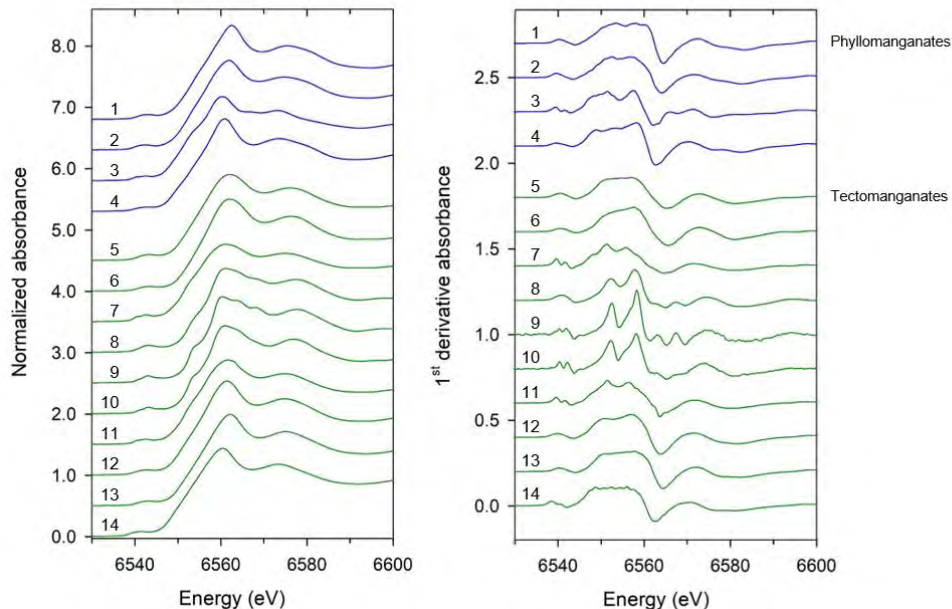
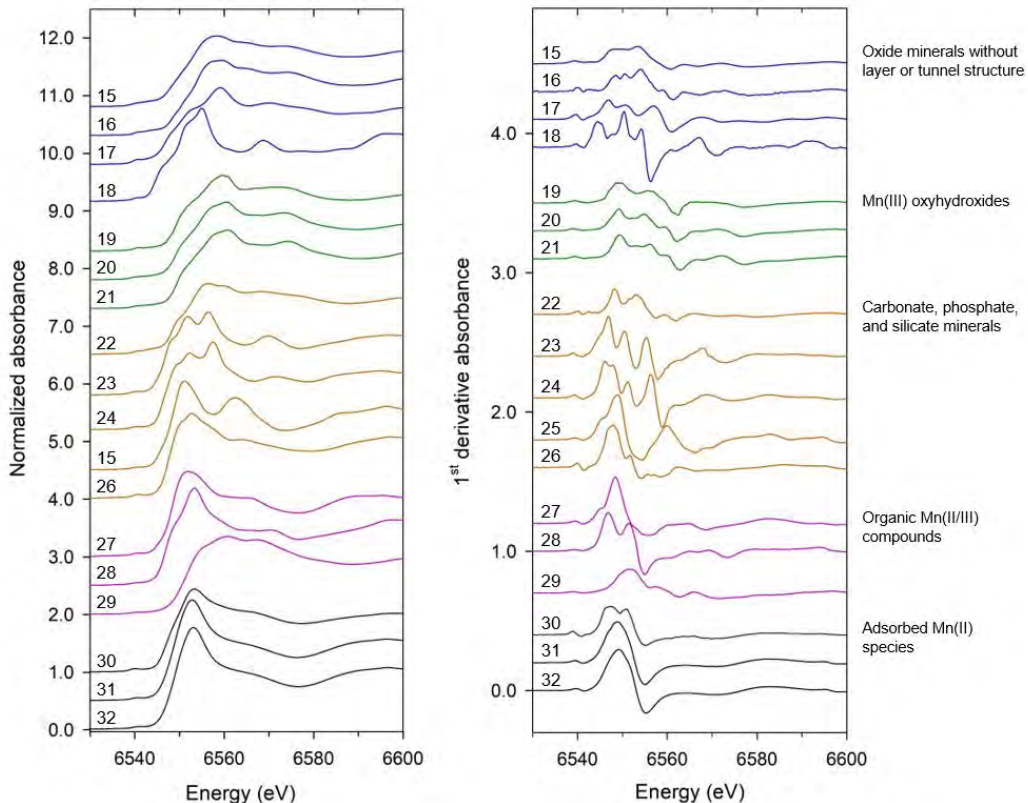


Figure 3



Always consult and cite the final, published document. See <http://www.minsocam.org> or GeoscienceWorld

Figure 4

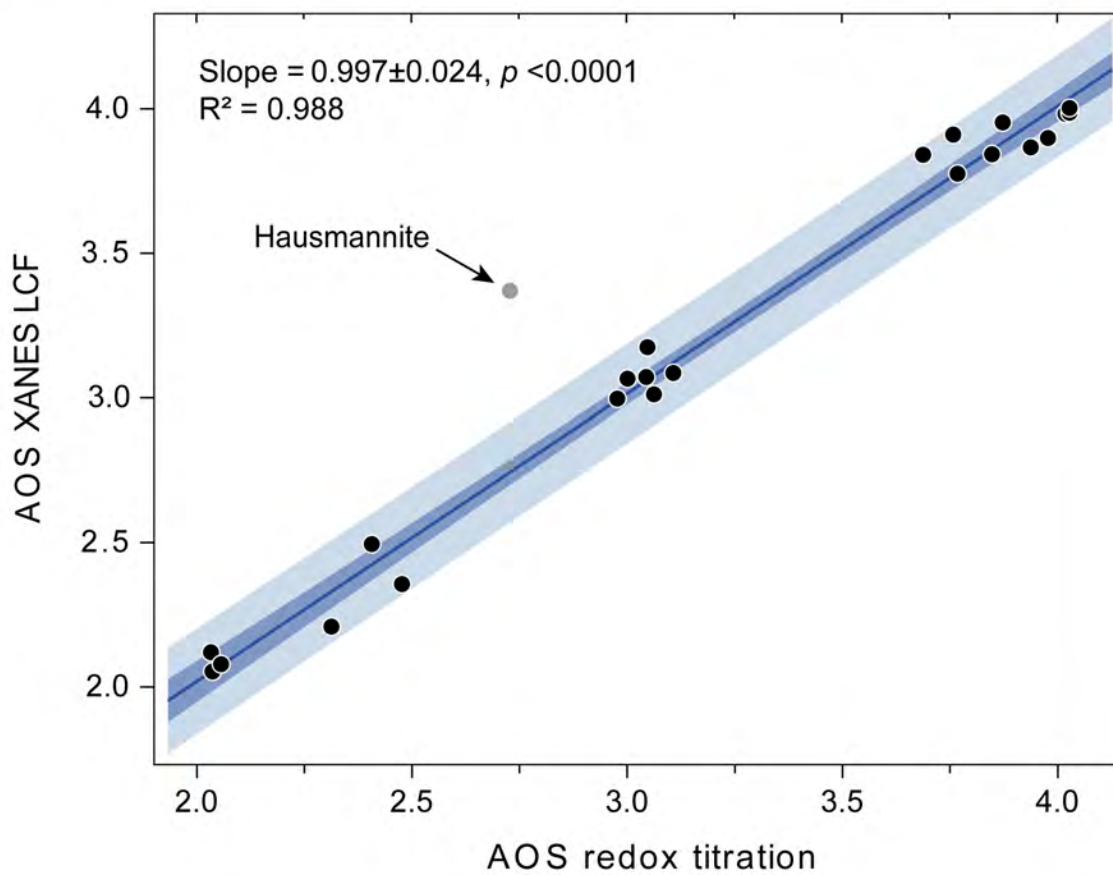


Figure 5

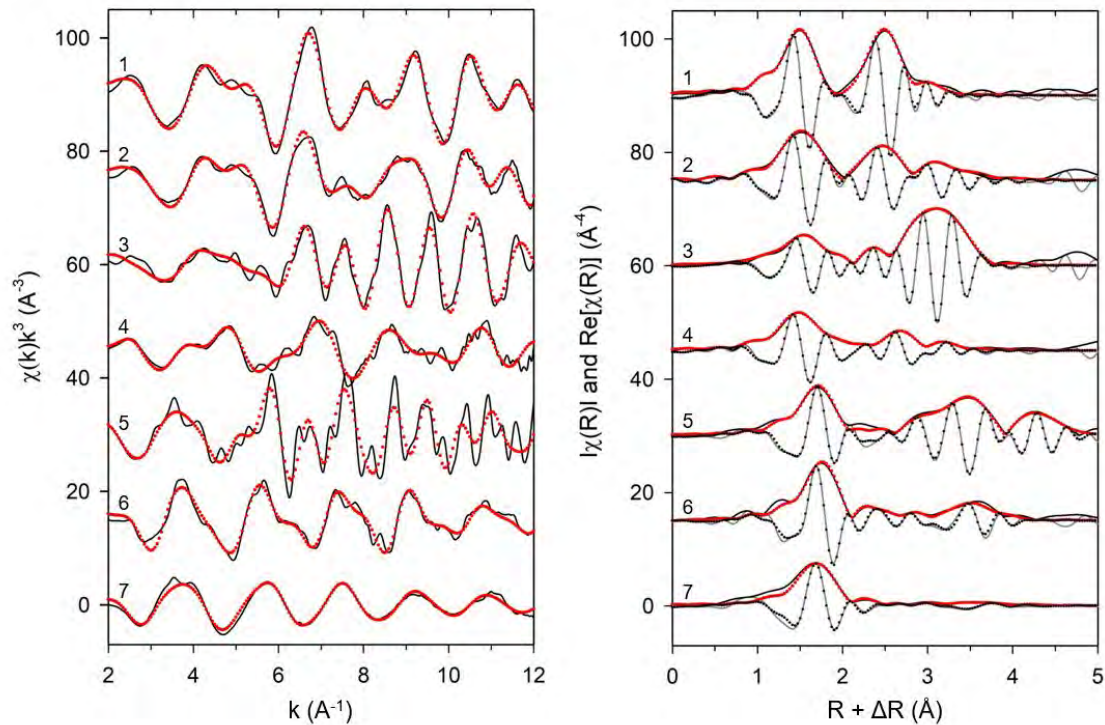




Figure 6

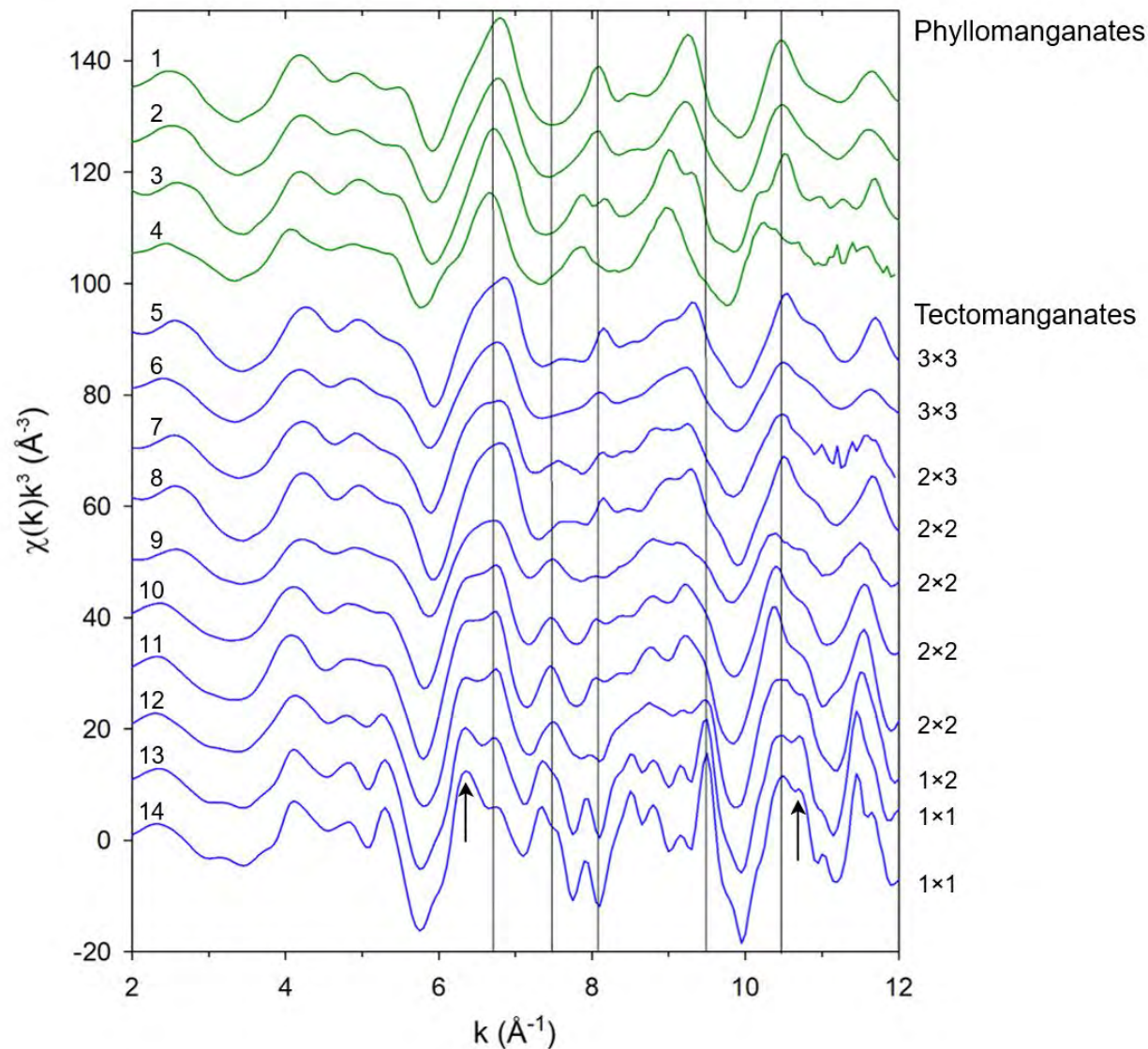


Figure 7

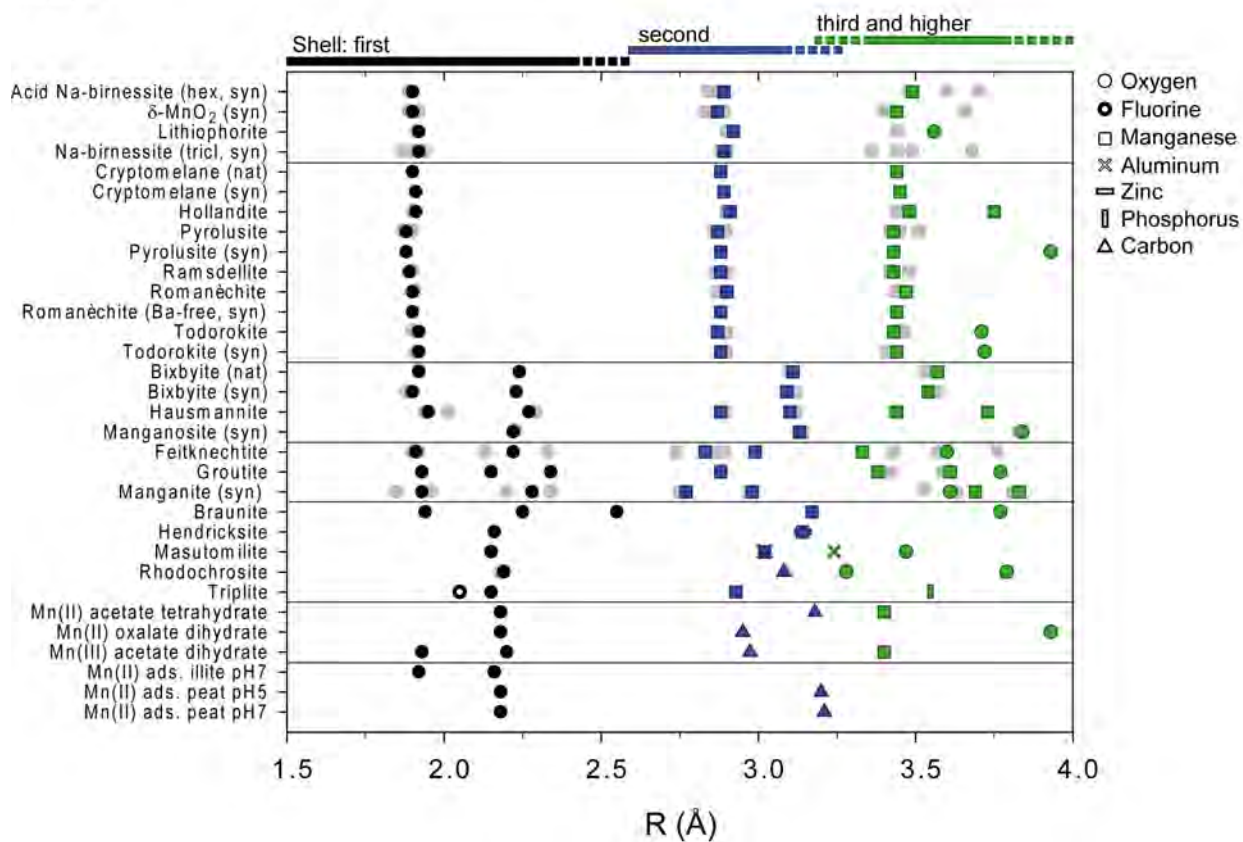


Figure 8

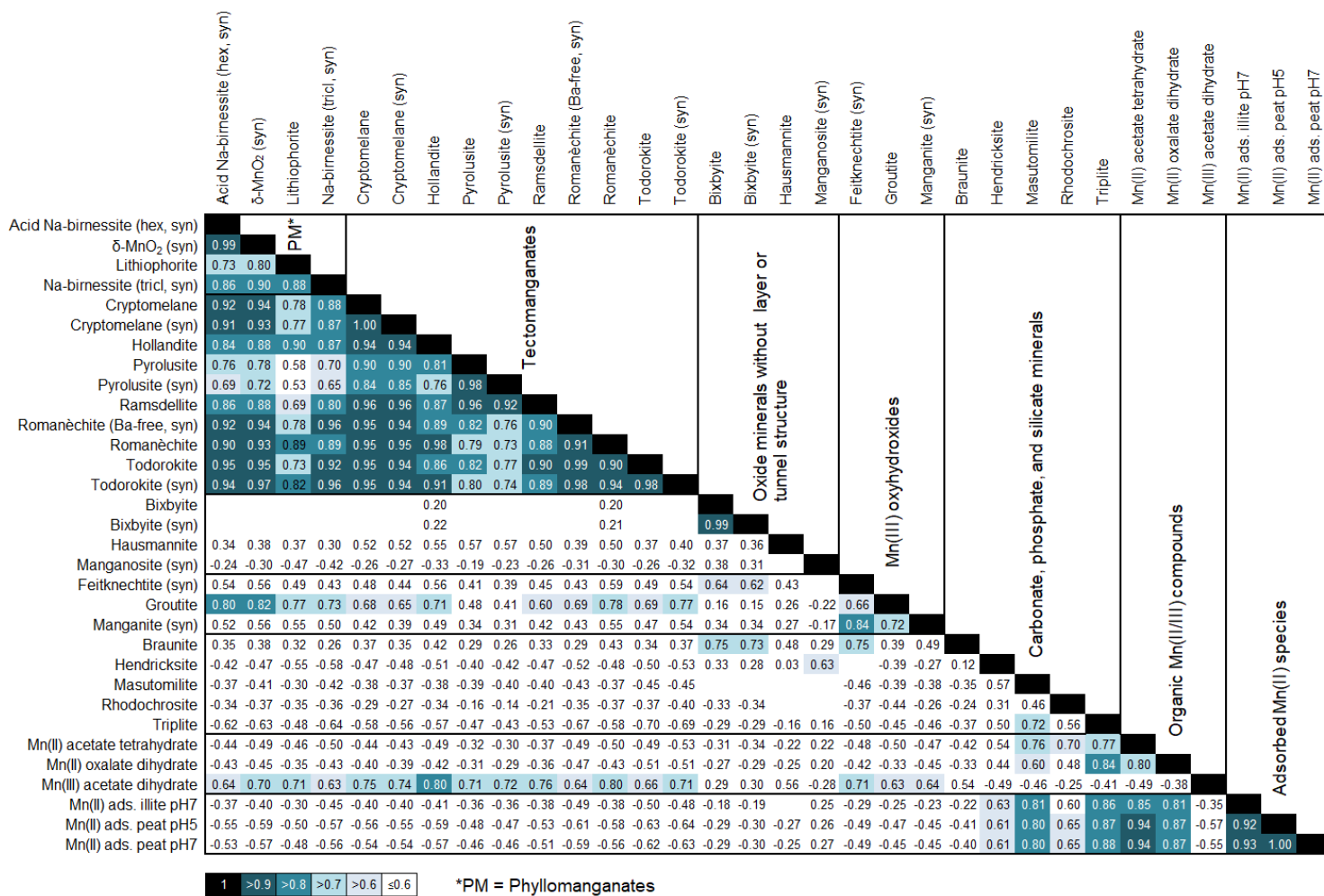




Figure 9

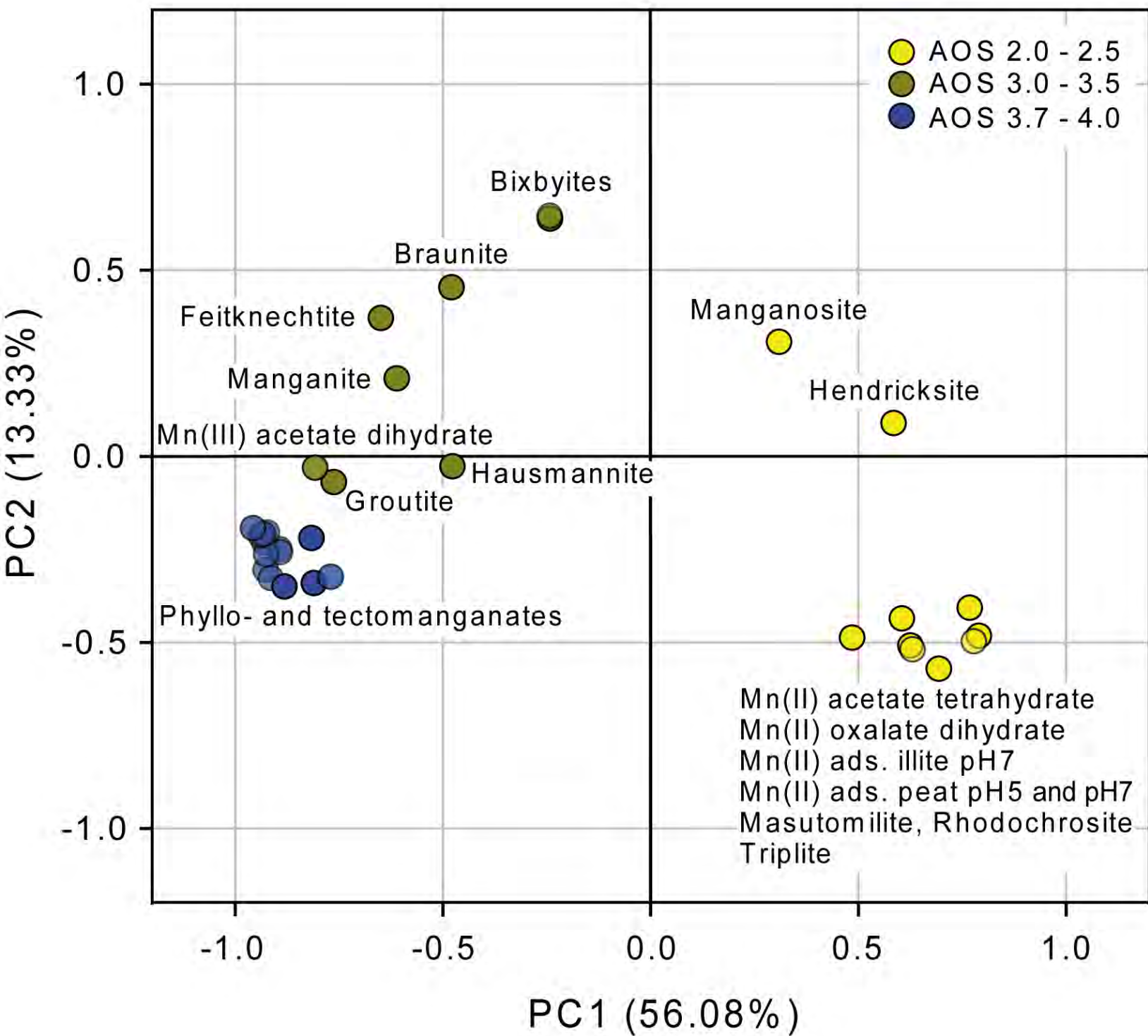


Figure 10

